Liquid and Ice Cloud Microphysics in the CSU General Circulation Model. Part I: Model Description and Simulated Microphysical Processes

LAURA D. FOWLER, DAVID A. RANDALL, AND STEVEN A. RUTLEDGE

Department of Atmospheric Science, Colorado State University, Fort Collins, Colorado

(Manuscript received 30 March 1994, in final form 21 July 1995)

ABSTRACT

Microphysical processes responsible for the formation and dissipation of water and ice clouds have been incorporated into the Colorado State University General Circulation Model in order to 1) yield a more physically based representation of the components of the atmospheric moisture budget, 2) link the distribution and optical properties of the model-generated clouds to the predicted cloud water and ice amounts, and 3) produce more realistic simulations of cloudiness and the earth's radiation budget.

The bulk cloud microphysics scheme encompasses five prognostic variables for the mass of water vapor, cloud water, cloud ice, rain, and snow. Graupel and hail are neglected. Cloud water and cloud ice are predicted to form through large-scale condensation and deposition processes and also through detrainment at the tops of cumulus towers. The production of rain and snow occur through autoconversion of cloud water and cloud ice. Rain drops falling through clouds can grow by collecting cloud water, and falling snow can collect both cloud water and cloud ice. These collection processes are formulated using the continuous collection equation. Evaporation of cloud water, cloud ice, rain, and snow are allowed in subsaturated layers. Melting and freezing are included. We also provide a coupling between convective clouds and stratiform anvils through the detrainment of cloud water and cloud ice at the tops of cumulus towers. Interactive cloud optical properties provide the link between the cloud microphysics and radiation parameterizations; the optical depths and infrared emissivities of large-scale stratiform clouds are parameterized in terms of the cloud water and cloud ice paths.

Two annual-cycle numerical simulations are performed to assess the impact of cloud microphysics on the hydrological cycle. In the "EAULIQ" run, large-scale moist processes and cloud optical properties are driven by the bulk cloud microphysics parameterization. In the "CONTROL" run, condensed water is immediately removed from the atmosphere in the form of rain, which may evaporate as it falls through subsaturated layers. Stratiform ice clouds are not considered in CONTROL. When clouds are present, cloud optical depths and cloud infrared emissivities are dependent on the mean cloud temperatures.

Results are presented in terms of January and July monthly averages. Emphasis is placed on the spatial distributions of cloud water, cloud ice, rain, and snow produced by the cloud microphysics scheme. In EAULIQ, cloud water and cloud ice are more abundant in the middle latitudes than in the Tropics, suggesting that large-scale condensation contributes a major part to the production of condensed water. Comparisons between the simulated vertically integrated cloud water and the columnar cloud water retrievals from satellite microwave measurements over the global oceans indicate a reasonable agreement. Interactions between the cloud microphysics and cumulus convection parameterizations lead to smaller, more realistic precipitation rates. In particular, the cumulus precipitation rate is strongly reduced when compared to CONTROL.

1. Introduction

Clouds are one of the key climate system components affecting the dynamics of the atmosphere through complex couplings among radiative, thermodynamic, and dynamic processes (Arakawa 1975). Interactions between clouds and radiation and between clouds and the hydrological cycle are inadequately understood. Realistic parameterizations of these interactions in terms of cloud microphysical processes and cloud radiative properties are only now being developed for use in atmospheric general circulation models (GCMs). Such parameterizations are needed in order to assess the effects of clouds on climate, especially in the context of climate change studies.

The development of cloud parameterizations and the simulation of the numerous interactions among cloudiness, radiation, and the hydrologic cycle have been continuing challenges since the very first global atmospheric models. Historically, four ways of representing clouds in GCMs may be distinguished.

1) The earliest "fixed cloud" approach uses a fixed geographical distribution of the cloud fraction and cloud optical depths, compiled from early satellite and ground-based observations (e.g., Manabe et al. 1965; Smagorinsky et al. 1965; Washington and Kasahara 1970; Holloway and Manabe 1971; Mac Avaney et al.

Corresponding author address: Dr. Laura D. Fowler, Department of Atmospheric Science, Colorado State University, Fort Collins, CO 80523.

1978). In these early models, clouds were not allowed to influence climate except through essentially prescribed short- and longwave radiative effects.

2) "Early diagnostic" cloud parameterizations predicted the occurrence of clouds based on a prescribed saturation threshold of the relative humidity, as suggested by Smagorinsky (1960). The cloud fraction was diagnosed as a function of selected large-scale variables, such as relative humidity, vertical velocity, or rate of precipitation, introducing a dependence of the predicted cloudiness on the predicted large-scale moisture field. The cloud optical properties were prescribed as functions of cloud type (most often convective versus large scale) and cloud height. Climates simulated by GCMs using this kind of cloud parameterization have been described in detail by Hansen et al. (1983), Slingo (1985), Williamson et al. (1987), and Wetherald and Manabe (1988), among others.

3) The "post-Somerville–Remer" (1984) approach parameterized cloud formation in the same way as the "early diagnostic" approach. The important change was that cloud optical properties were parameterized as functions of temperature, adding a potentially important new feedback between the variations in cloudiness and climate in response to external climate forcing (e.g., Paltridge 1980; Charlock 1982; Somerville and Remer 1984). The parameterization of cloud optical depth in terms of temperature was based on observational and theoretical evidence that the cloud water and ice contents vary with temperature (Feigelson 1978; Betts and Harshvardhan 1987; Platt and Harshvardhan 1988) and that cloud optical depth is, as a first approximation, proportional to cloud water and ice paths (Stephens 1978). Cloud parameterizations using these concepts were described by Coiffier et al. (1987), Harshvardhan et al. (1989), Morcrette (1991), and McFarlane et al. (1992).

4) The "prognostic cloud water" approach includes prognostic equations for the cloud water and/or ice contents, which are used to simulate the temporal and spatial variations of cloudiness due to cloud microphysical processes (Sundqvist 1978). The use of prognostic condensate variables introduces a memory for the cloud system. Cloud optical properties are again parameterized in terms of the liquid water and ice paths. This promising approach to cloud parameterization is used in the present study and is described in greater detail below.

How do emerging GCMs with prognostic cloud water parameterizations attempt to simulate the interactions among cloud dynamics, cloud microphysics, and radiative processes? Some elements of the approach are as follows.

1) *Prediction of the total atmospheric condensed water and its partitioning between cloud water and cloud ice, with the aim to simulate the life cycles of water and ice clouds.* Separate treatment of the water and ice phases is highly advantageous because they undergo significantly different microphysical and thermodynamical processes, precipitate at different rates, and have different optical properties. A major difficulty arises in testing the global simulated cloud water and ice amounts against observations. Whereas satellite observations of columnar water content over the oceans are available (Njoku and Swanson 1983; Prabhakara et al. 1983; Greenwald et al. 1993), similar observations of cloud ice are almost nonexistent. Bauer and Schluessel (1993) obtained the global distribution of the ice water path over the oceans for August 1987 using a radiative transport model applied to microwave radiances from the Special Sensor Microwave Imager (SSM/I). The retrieval of the ice water path was found to be problematic because of the strong gradient of scattering efficiency with crystal sizes. Lin and Rossow (1994) provided one month of zonally averaged estimates of the ice water path for cold nonprecipitating clouds from collocated ISCCP[1] and SSM/I radiances. They defined the ice water path as the difference between the total water path derived from ISCCP shortwave radiances and the liquid water path derived from SSM/I microwave radiances. Both results are very preliminary. In situ ice data are available based on local cloud ice measurements obtained in regional experiments such as FIRE[2] (e.g., Heymsfield and Donner 1990) and ICE[3] (Raschke et al. 1990). Such in situ data are difficult to compare with simulated large-scale averages.

2) *Explicit coupling between the large-scale condensation and cumulus convection parameterizations with the aim to improve the simulation of stratiform anvil clouds formed at the tops of cumulus towers.* As stressed by Randall (1989), the parameterization of anvil clouds and cirrus debris arising from cumulus activity remains one of the most serious weaknesses of GCM cloud parameterizations. Fowler and Randall (1994) argue that anvil clouds act as regulators of the hydrologic cycle by providing a global negative feedback between atmospheric radiative cooling and convective activity. To simulate the coupling between cumulus updrafts and upper-tropospheric stratiform clouds, Del Genio and Yao (1990), Ose (1993), and Tiedtke (1993) add the detrained condensed water to the prognostic stratiform cloud water.

3) *Physically based parameterizations of the various cloud microphysical processes, such as conversion of cloud water and ice to water vapor in subsaturated air and conversion of cloud water and ice to rain and snow in supersaturated air.* Many parameterizations in current use still assume that evaporation occurs instan-

[1] ISCCP: International Satellite Cloud Climatology Project.
[2] FIRE: First International Satellite Cloud Climatology Project (ISCCP) Regional Experiment.
[3] ICE: International Cirrus Experiment.

taneously and that large-scale and convective condensation lead to instantaneous and complete rainout. It has been shown that such a simplified treatment of the hydrologic cycle produces an unrealistic "blinking" of the cloudiness and an enhanced unrealistic variability of the top of the atmosphere components of the planetary radiation budget (Charlock et al. 1988; Smith and Vonder Haar 1991). This increased variability is further enhanced when the diurnal cycle of clouds and radiation is neglected.

4) *Physically based parameterizations of cloud optical properties and fractional cloud amount.* The cloudy fraction of a GCM grid box depends on the subgrid-scale distributions of liquid water and ice. The problem of subgrid-scale cloudiness has not yet been adequately addressed in global models.

At present, several GCMs include one or more prognostic equations for the mass of cloud water and/or cloud ice, as well as an explicit description of the conversion rates between water vapor, cloud water, cloud ice, and precipitation. These models are listed in Table 1. The table shows that three classes of prognostic cloud parameterizations for GCMs may be distinguished:

The first class has its roots in the pioneering work of Sundqvist (1978), who proposed the use of a prognostic equation for cloud water with the goal to improve the parameterization of condensation in large-scale numerical models. He wrote that his purpose was "*. . . to design a fairly simple condensation model yielding not only the release of latent heat and precipitation but also cloud mass, for possible use in a large-scale dynamical model. . . .*"

The chief characteristics of Sundqvist-style cloud parameterizations are as follows. First, clouds form before the relative humidity reaches 100%, hence allowing for subgrid-scale cloud cover. The cloud parameterization uses a prescribed threshold relative humidity at which condensation is assumed to start, and the relative humidity in the cloud-free area is assume to increase linearly with the cloud cover. Using these assumptions, the cloud fraction may be expressed as a simple function of the relative humidity in the grid box (Sundqvist et al. 1989). Second, the model includes a prognostic equation for the mass of the total condensed water. The rate of change of the condensed water results from condensation of water vapor that may occur in the cloud-free and cloudy parts of the box, minus evaporation and precipitation that may occur in the cloudy part of the box. The condensation rate depends on the large-scale relative humidity and the moisture flux convergence. Precipitation and evaporation are parameterized in highly idealized ways. For instance, one equation is used to describe simultaneously autoconversion and collection processes. Because this class of prognostic cloud schemes uses only one prognostic equation to describe the temporal evolution of the condensed water, additional assumptions are needed to distinguish between the water and ice phases. Empirical functions of temperature are used to produce a smooth transition between the water and ice states when they coexist (Del Genio and Yao 1990; Sundqvist 1993). Cloud parameterizations of the Sundqvist type vary widely in complexity. Del Genio and Yao (1990) and Roeckner et al. (1990) followed the formulation of Sundqvist (1978) and Sundqvist et al. (1989) in terms of the continuity equation for the mass of the condensed water, formulation of the cloud fraction, and parameterizations of the precipitation and evaporation processes. Le Treut and Li (1988) combined a prognostic equation for the cloud liquid water with a simple top-hat probability distribution for the total water content (specific humidity plus condensed water specific content) within the grid box. The cloud fraction depends on a tunable parameter representing the variability of total water content about its mean value. More recently, Tiedtke (1993) developed fully prognostic equations for both cloud cover and total condensed water, taking into account advective processes, and sources and sinks due to parameterized diabatic processes in the European Centre for Medium-Range Weather Forecasts (ECMWF) model. Tiedtke's parameterizations of the precipitation processes and the microphysics of the ice and mixed phases are based on Sundqvist (1978) and Sundqvist (1993), respectively.

The second class of prognostic cloud water parameterizations accounts for the subgrid-scale distribution of the water vapor, condensed water, and temperature in the model grid box. Heise (1984) developed a statistical determination of both cloud cover and cloud water for the Deutscher Wetterdienst Model, based on the statistical cloud model of Sasamori (1975). Smith (1990) similarly adopted the concept of a statistical distribution of moist-conservative variables about their gridbox means to compute the cloud water content and cloud amount, following methods similar to those proposed by Sommeria and Deardorff (1977) and Mellor (1977). Ricard and Royer (1993) developed a statistical scheme that calculated simultaneously the cloud fraction, the liquid water content, the rate of condensation, and vertical diffusion based on the work of Mellor (1977) and Bougeault (1981).

The third class of prognostic cloud water parameterizations for GCMs uses minimally modified versions of bulk cloud microphysics equations originally developed for mesoscale cloud models. In contrast to Sundqvist-style parameterizations, these cloud parameterizations introduce separate prognostic equations for the mass of cloud water and cloud ice. In the most complex schemes, the details of the precipitation and evaporation processes are formulated using the continuous collection equations. Ghan and Easter (1992) tested the cloud microphysics package of the Colorado State University Regional Atmospheric Modeling System ("RAMS"; Cotton et al. 1982; Flatau et al. 1989)

TABLE 1. Survey of prognostic cloud water and cloud ice parameterizations for stratiform cloud parameterizations in GCMs.

Study	Stratiform clouds	Convective clouds	Cloud fraction	Cloud optics
First class:				
Sundqvist (1978)	Water phase only. The water content depends upon the large-scale saturation plus the local moisture flux convergence. Cloud microphysics is highly parameterized.	Not included.	Obtained from prognostic relative humidity plus prescribed relative humidity threshold.	Not included.
Le Treut and Li (1988)	Assumes a top-hat probability distribution of the total water content within the grid box	Moist adiabatic adjustment, plus Kuo-type schemes (Laval et al. 1981). No interactions with the large-scale condensation.	Depends on a tunable parameter.	Follows Stephens (1978).
Del Genio and Yao (1990)	Loosely based on Sundqvist (1978) and Sundqvist et al. (1989). Includes a mixed and ice phase.	Del Genio and Yao (1988). Detrained convective condensate is added to stratiform cloud water.	Fractional cloudiness depends on relative humidity (Sundqvist et al. 1989).	Follows Stephens (1978).
Roeckner et al. (1990)	Loosely based on Sundqvist (1978) and Sundqvist et al. (1989). Includes a mixed and ice phase.	No interactions between upper-tropospheric stratiform anvils and convective clouds.	Fractional cloudiness (Sundqvist et al. 1989).	Not specified.
Tiedtke (1993)	Prognostic cloud water–ice equations that include all the sources and sinks due to diabatic processes.	Mass-flux scheme (Tiedtke 1989). Convective clouds act as sources of stratiform cloud mass.	Prognostic cloud fraction equation that include all the sources and sinks due to diabatic processes.	Follows Morcrette (1991).
Second class:				
Heise (1984)	Water phase only. Based on the statistical cloud model of Sasamori (1975).	Penetrative convection according to Kuo (1965).	Depends upon a normal distribution with mean cloud height $\bar{z}$ and standard deviation σ_z (Sasamori 1975).	Follows Stephens (1978).
Smith (1990)	Assumes a statistical distribution of the water content about its gridbox mean value, loosely following Sommeria and Deardorff (1977).	Includes the effects of turbulent mixing in clouds. No interactions with deep convection.	Assumes a statistical distribution of the cloud amount about its gridbox mean value, following Sommeria and Deardorff (1977).	Prescribed.
Ricard and Royer (1993)	Water phase only. Uses the subgrid-scale condensation scheme of Mellor (1977) and Bougeault (1981).	Mass-flux scheme (Bougeault 1985).	Simultaneously computed with the water content assuming a Gaussian distribution of the conservative variables following Mellor (1977) and Bougeault (1981).	Not specified.
Third class:				
Ghan and Easter (1992)	Adapted from CSU-RAMS cloud microphysics package (Cotton et al. 1982). Precipitation is diagnostic.	Not specified	Not specified.	Not specified.
Ose (1993)	Simplified bulk cloud microphysics scheme.	Arakawa–Shubert (1974). Convective condensate is added to the stratiform cloud water and ice.	No fractional cloudiness. Cloud fraction is set equal to 0 or 1.	Follows Stephens (1978) for water clouds and Liou and Wittman (1979) for ice clouds.
This study	Adapted from Rutledge and Hobbs (1983) and Lin et al. (1983) bulk cloud microphysics equations.	Uses modified Arakawa–Schubert (1974).	No fractional cloudiness. Cloud fraction is set equal to 0 or 1.	Follows Stephens (1978).

using a single column model driven by vertical motions characteristics of those resolved by a GCM. They emphasized difficulties resulting from differences in the temporal and spatial resolution between mesoscale and large-scale models. In particular, they showed that the inclusion of a "diagnostic" versus "prognostic" equation for the precipitation species and instantaneous melting of snow allow the use of a longer time step without significantly affecting the model's ability to simulate the temporal evolution of the cloud water and ice variables. Ose (1993) included separate prognostic variables for the mass of cloud water and cloud ice and incorporated simple cloud microphysical processes into the UCLA GCM in order to study the distribution and radiative properties of upper-tropospheric clouds. Like Ghan and Easter (1992), Ose (1993) diagnostically determined the amounts of rain and snow. His results highlight the very strong sensitivity of the distribution and radiative properties of tropical cirrus clouds to cloud microphysics. Ose (1993) assumed that the GCM grid box is overcast whenever cloud water or cloud ice is present.

A major advantage of using prognostic equations for the condensed species is that cloud optical properties can be parameterized as functions of the predicted cloud water and cloud ice paths, allowing a direct coupling between the hydrological cycle and radiative processes. This coupling has been shown to be extremely important in studying climate change due to external forcing (Senior and Mitchell 1993). Numerous efforts have been made to develop parameterizations of cloud optical properties for both the water and ice phases (e.g., Stephens 1978; Slingo 1989; Hu and Stamnes 1993; Ebert and Curry 1993).

In this paper, we describe a cloud microphysics scheme developed to improve the simulation of the hydrologic and radiation processes in the Colorado State University General Circulation Model (CSU GCM). The simulations of cloudiness and radiation are described in detail by Fowler and Randall (1996, hereafter Part II). Section 2 provides a complete description of the cloud microphysics scheme, while section 3 outlines the chief differences between the EAULIQ and CONTROL runs. The effects of the cloud microphysics scheme on the simulated hydrologic cycle are analyzed in section 4. Section 5 summarizes our results and highlights questions and issues to be addressed in future work.

2. Cloud microphysics

Our parameterization is based on the bulk cloud microphysics equations of mesoscale cloud models described by Lin et al. (1983) and Rutledge and Hobbs (1983, 1984). We introduce five prognostic moisture variables for the mixing ratios of water vapor, cloud water, cloud ice, rain, and snow. Cloud water and cloud ice are predicted to form through large-scale condensation and deposition processes. An important additional source of cloud water and cloud ice is detrainment at the tops of cumulus towers. As in the studies cited above, we assume that the fall speeds of cloud water and cloud ice particles are negligible. Rain and snow, of course, have nonnegligible fall velocities. A detailed description of the bulk cloud microphysics equations, including the fall speed formulation, is given in appendix A. Microphysical interactions among water vapor, cloud water, cloud ice, rain, and snow are represented schematically in Fig. 1. Acronyms that we have adopted as short names for the various microphysical processes are listed in Table 2.

At present, our cloud microphysics parameterization does not include a prognostic equation for the number concentration of cloud water droplets and cloud ice crystals. This simplification allows us to express the rate of condensation of water vapor to cloud water and the rate of deposition of water vapor to cloud ice as a function of the large-scale supersaturation. In so doing, we do not distinguish between homogeneous and heterogeneous nucleation for the ice phase. We assume that there always exist sufficient nuclei to initiate condensation and deposition. Parameterizations of cloud droplet nucleation for use in large-scale numerical models are currently being tested (Ghan et al. 1993, 1994).

Water vapor is a source of cloud water (PCOND) and cloud ice (PSUB). Cloud water is assumed to form by condensation when the temperature (T) is greater than or equal to $T_0 = 0$°C and the air is supersaturated with respect to water. Cloud ice is predicted to form by deposition of vapor if $T < T_{00}$ and the air is supersaturated with respect to ice. Supercooled cloud water and cloud ice are allowed to coexist in the temperature range $T_{00} \leq T < T_0$ (PBERG). Here we choose $T_{00} = -20$°C. Water vapor can also be converted to rain and snow by condensation (PREVP) and deposition (PSEVP), respectively.

Cloud water is a source for water vapor through evaporation in a subsaturated layer (PCOND) or a source of rain if the air remains supersaturated. The conversion of cloud water to rain occurs through two different mechanisms: 1) autoconversion of cloud water to rain (PRAUT) and 2) collection of cloud water by rain (PRACW). Supercooled cloud water is also a source for snow by riming (PSACW), and it can be a source of cloud ice through the Bergeron process ($T_{00} \leq T < T_0$) or instantaneous freezing ($T < T_{00}$).

Cloud ice is a source of water vapor by sublimation when the air is subsaturated with respect to ice (PSUB). Cloud ice is a source for snow through two different mechanisms: 1) autoconversion of cloud ice to form snow (PSAUT) and 2) collection of cloud ice by snow (PSACI). Instantaneous melting of cloud ice to form cloud water occurs if $T \geq T_0$ (PSMLTI).

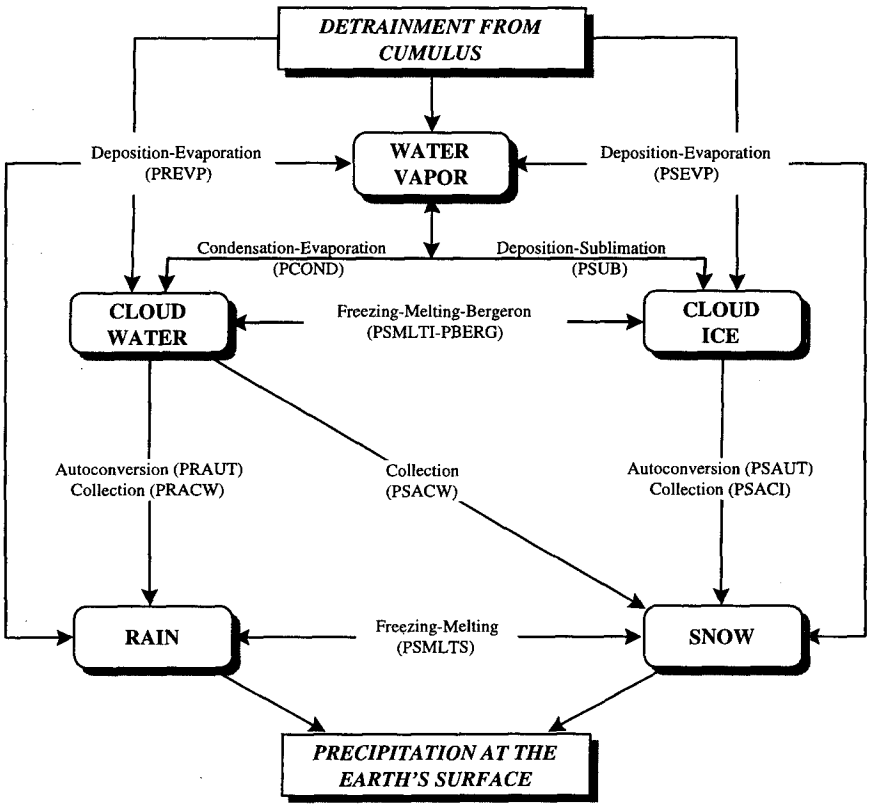

FIG. 1. Schematic diagram of cloud microphysics processes.

Rain is a source for water vapor by evaporation (PREVP). Rain may also be a source for snow by instantaneous freezing if $T < T_0$ (PSMLTS).

Snow is a source for water vapor by sublimation (PSEVP). Also, snow may be a source of rain by instantaneous melting (PSMLTS) as it falls through the 0°C level.

TABLE 2. Keys to Fig. 1.

Symbol	Microphysical process
PBERG	Bergeron process
PCOND	Condensation/evaporation of water vapor
PRACW	Collection of cloud water by rain
PRAUT	Autoconversion of cloud water to rain
PREVP	Deposition of water vapor on rain/evaporation of rain
PSACI	Collection of cloud ice by snow
PSACW	Collection of supercooled cloud water by snow
PSAUT	Autoconversion of cloud ice to snow
PSEVP	Deposition of water vapor on snow/evaporation of snow
PSMLTI	Melting of cloud ice/freezing of cloud water
PSMLTS	Melting of snow/freezing of rain
PSUB	Deposition of water vapor on cloud ice/sublimation of cloud ice

a. Continuity equations

The CSU GCM uses a modified σ coordinate (Suarez et al. 1983) to represent the vertical structure of the atmosphere. Continuity equations for the mixing ratios of water vapor (q_v), cloud water (q_c), cloud ice (q_i), rain (q_r), snow (q_s), and the potential temperature (θ) on a σ surface may be respectively written as follows:

$$\frac{\partial}{\partial t}(\pi^* q_v) + \nabla\cdot(\pi^* \mathbf{V} q_v) + \frac{\partial}{\partial \sigma}(\pi^* \dot{\sigma} q_v) = \pi^*(\mathrm{SCM}_v + \mathrm{SCUP}_v + \mathrm{SCMADJ}_v + \mathrm{SDADJ}_v + \mathrm{STB}_v), \quad (1)$$

$$\frac{\partial}{\partial t}(\pi^* q_c) + \nabla\cdot(\pi^* \mathbf{V} q_c) + \frac{\partial}{\partial \sigma}(\pi^* \dot{\sigma} q_c) = \pi^*(\mathrm{SCM}_c + \mathrm{SCUP}_c), \quad (2)$$

$$\frac{\partial}{\partial t}(\pi^* q_r) + \nabla\cdot(\pi^* \mathbf{V} q_r) + \frac{\partial}{\partial \sigma}(\pi^* \dot{\sigma} q_r) = \pi^*\left[\mathrm{SCM}_r + \mathrm{SCUP}_r + g\frac{1}{\pi^*}\frac{\partial}{\partial \sigma}(\rho V_r q_r)\right], \quad (3)$$

$$\frac{\partial}{\partial t}(\pi^* q_i) + \nabla\cdot(\pi^* \mathbf{V} q_i) + \frac{\partial}{\partial \sigma}(\pi^* \dot{\sigma} q_i) = \pi^*(\mathrm{SCM}_i + \mathrm{SCUP}_i), \quad (4)$$

$$\frac{\partial}{\partial t}(\pi^* q_s) + \nabla\cdot(\pi^* \mathbf{V} q_s) + \frac{\partial}{\partial \sigma}(\pi^* \dot{\sigma} q_s) = \pi^*\left[\mathrm{SCM}_s + \mathrm{SCUP}_s + g\frac{1}{\pi^*}\frac{\partial}{\partial \sigma}(\rho V_s q_s)\right], \quad (5)$$

and

$$\frac{\partial}{\partial t}(\pi^* \theta) + \nabla\cdot(\pi^* \mathbf{V}\theta) + \frac{\partial}{\partial \sigma}(\pi^* \dot{\sigma}\theta) = \pi^* \frac{\theta}{c_p T}(\mathrm{SCM}_T + \mathrm{SCUP}_T + \mathrm{SCMADJ}_T + \mathrm{SDADJ}_T + \mathrm{STB}_T + \mathrm{SRAD}_T). \quad (6)$$

In (1)–(6), $\nabla\cdot(\ )$ denotes the operator on a σ surface, π^* is the pressure scale used with the definition of σ (see Suarez et al. 1983), V is the horizontal wind vector, $\dot{\sigma}$ is the vertical velocity, and g is the gravitational acceleration. SCM_x, SCUP_x, SCMADJ_x, SDADJ_x, STB_x, and SRAD_x represent the rates of change in q_x and θ due to cloud microphysical processes, cumulus convection, moist convective adjustment, dry convective adjustment, turbulent mixing, and radiation processes, respectively (here x refers to the subscripts v, c, r, i, s, and T). In (3) and (5), $g\partial/\partial\sigma(\rho V_x q_x)$ represents the vertical divergence of rain or snow with fall speed V_x. SCUP_r and SCUP_s are set equal to zero because we assume that condensed water may only be detrained in the form of cloud water and cloud ice. Other symbols are listed in appendix B.

In terms of the cloud microphysical processes listed in Table 2, the source terms SCM_v, SCM_c, SCM_r, SCM_i, SCM_s, and SCM_T may be expressed by the following equations:

$$\mathrm{SCM}_v = -\delta_1\left[\gamma_1\frac{q_v - q_{sw}}{\tau_w} + \gamma_2\frac{q_v - q_{sm}}{\tau_m} + \gamma_3\frac{q_v - q_{si}}{\tau_i}\right] - \delta_1[\gamma_1(S_w - 1)\,\mathrm{FRV}\,q_r + \gamma_2(S_m - 1)\,\mathrm{FSV}\,q_s + \gamma_3(S_i - 1)\,\mathrm{FSV}\,q_s] - \delta_2\left[\gamma_1\frac{S_w - 1}{\tau_w}q_c + \gamma_2\frac{S_m - 1}{\tau_m}(q_c + q_i) + \gamma_3\frac{S_i - 1}{\tau_i}q_i\right] - \delta_2[\gamma_1(S_w - 1)\,\mathrm{FRV}\,q_r + \gamma_2(S_m - 1)\,\mathrm{FSV}\,q_s + \gamma_3(S_i - 1)\,\mathrm{FSV}\,q_s] \quad (7)$$

$$\mathrm{SCM}_c = \delta_1\left[\gamma_1\frac{q_v - q_{sw}}{\tau_w} + \gamma_2\omega\frac{q_v - q_{sm}}{\tau_m}\right] + \delta_2\left[\gamma_1\frac{S_w - 1}{\tau_w}q_c + \gamma_2\omega\frac{S_m - 1}{\tau_m}(q_c + q_i)\right] - \gamma_1\alpha(q_c - q_{c0}) - \gamma_1\,\mathrm{FCR}\,q_c q_r - \gamma_2\,\mathrm{FCS}\,q_c q_s + \frac{q_i}{\Delta t}(T \geqslant T_0) - \frac{q_c}{\Delta t}(T < T_{00}), \quad (8)$$

$$\mathrm{SCM}_r = \delta_1\gamma_1(S_w - 1)\,\mathrm{FRV}\,q_r + \delta_2\gamma_1(S_w - 1)\,\mathrm{FRV}\,q_r + \gamma_1\alpha(q_c - q_{c0}) + \gamma_1\,\mathrm{FCR}\,q_c q_r + \frac{q_s}{\Delta t}(T \geqslant T_0) - \frac{q_r}{\Delta t}(T < T_0), \quad (9)$$

$$\mathrm{SCM}_i = \delta_1\left[\gamma_2(1 - \omega)\frac{q_v - q_{sm}}{\tau_m} + \gamma_3\frac{q_v - q_{si}}{\tau_i}\right] + \delta_2\left[\gamma_2(1 - \omega)\frac{S_m - 1}{\tau_m}(q_c + q_i) + \gamma_3\frac{S_i - 1}{\tau_i}q_i\right] - (\gamma_2 + \gamma_3)\beta(q_i - q_{i0}) - (\gamma_2 + \gamma_3)\,\mathrm{FIS}\,q_i q_s - \frac{q_i}{\Delta t}(T \geqslant T_0) + \frac{q_c}{\Delta t}(T < T_{00}), \quad (10)$$

$$\mathrm{SCM}_s = \delta_1[\gamma_2(S_m - 1)\,\mathrm{FSV}\,q_s + \gamma_3(S_i - 1)\,\mathrm{FSV}\,q_s] + \delta_2[\gamma_2(S_m - 1)\,\mathrm{FSV}\,q_s + \gamma_3(S_i - 1)\,\mathrm{FSV}\,q_s] + (\gamma_2 + \gamma_3)\beta(q_i - q_{i0}) + (\gamma_2 + \gamma_3)\,\mathrm{FIS}\,q_i q_s + \gamma_2\,\mathrm{FCS}\,q_c q_s - \frac{q_s}{\Delta t}(T \geqslant T_0) + \frac{q_r}{\Delta t}(T < T_0), \quad (11)$$

and

$$\mathrm{SCM}_T = \delta_1\left[\gamma_1\frac{L_c}{c_p}\frac{q_v - q_{sw}}{\tau_w} + \gamma_2\frac{L_m}{c_p}\frac{q_v - q_{sm}}{\tau_m} + \gamma_3\frac{L_s}{c_p}\frac{q_v - q_{si}}{\tau_i}\right] + \delta_2\left[\gamma_1\frac{L_c}{c_p}\frac{S_w - 1}{\tau_w}q_c + \gamma_2\frac{L_m}{c_p}\frac{S_m - 1}{\tau_m}(q_c + q_i) + \gamma_3\frac{L_s}{c_p}\frac{S_i - 1}{\tau_i}q_i\right]$$

$$+ \delta_1\left[\gamma_1 \frac{L_c}{c_p}(S_w - 1)\,\mathrm{FRV}\,q_r + \gamma_2 \frac{L_m}{c_p}(S_m - 1)\,\mathrm{FSV}\,q_s + \gamma_3 \frac{L_s}{c_p}(S_i - 1)\mathrm{FSV}\,q_s\right]$$

$$+ \delta_2\left[\gamma_1 \frac{L_c}{c_p}(S_w - 1)\,\mathrm{FRV}\,q_r + \gamma_2 \frac{L_m}{c_p}(S_m - 1)\,\mathrm{FSV}\,q_s + \gamma_3 \frac{L_s}{c_p}(S_i - 1)\mathrm{FSV}\,q_s\right]$$

$$+ \frac{L_f}{c_p}\left[\frac{q_c}{\Delta t}(T < T_{00}) - \frac{q_i}{\Delta t}(T \geqslant T_0) + \frac{q_r}{\Delta t}(T < T_{00}) - \frac{q_s}{\Delta t}(T \geqslant T_0)\right]$$

$$+ \gamma_2 \frac{L_f}{c_p}\mathrm{FCS}\,q_c q_s (T < T_0). \quad (12)$$

Equations (7)–(12) are derived following (A46)–(A51) of appendix A and using the symbols listed in appendix B. These equations express the time rate of change of each species in terms of its interactions with the other species through the various microphysical processes for the water phase ($T \geqslant T_0$), the mixed phase ($T_{00} \leqslant T < T_0$), and the ice phase ($T < T_{00}$). Here S_w and S_i are the saturations with respect to water and ice; S_m is the mixed phase saturation obtained by using the interpolated saturation vapor pressure in the mixed-phase temperature range ($T_{00} \leqslant T < T_0$); τ_w, τ_i, and τ_m are prescribed relaxation times that are used to express condensation/evaporation and deposition/sublimation as finite but rapid microphysical processes [refer to (A11), (A12), (A25), (A26), (A44), and (A45) of appendix A]. They are independent of the cloud microphysics time step. Although we know that deposition/sublimation occurs at a slower rate than condensation/evaporation, we assume for simplicity that $\tau_w = \tau_i = \tau_m = 100$ s. Additional sensitivity experiments using different values of τ_w, τ_i, and τ_m are needed. In Eqs. (7)–(12), we use the notation

$$\delta_1 = 1, \delta_2 = 0 \quad \text{for} \quad S_{w,i,m} \geqslant 1$$
$$\delta_1 = 0, \delta_2 = 1 \quad \text{for} \quad S_{w,i,m} < 1 \quad (13)$$

to distinguish between supersaturation and subsaturation conditions and

$$\begin{aligned} &\gamma_1 = 1, \quad \gamma_2 = \gamma_3 = 0 \quad \text{for} \quad (T \geqslant T_0) \\ &\gamma_2 = 1, \quad \gamma_1 = \gamma_3 = 0 \quad \text{for} \quad (T_{00} \leqslant T < T_0) \\ &\gamma_3 = 1, \quad \gamma_1 = \gamma_2 = 0 \quad \text{for} \quad (T < T_{00}) \end{aligned} \quad (14)$$

to distinguish between the water, mixed, and ice phases for the microphysical processes that are not instantaneous; ω is a temperature-dependent weight that controls the partitioning between cloud water and cloud ice in mixed-phase clouds. FCR, FIS, and FCS are given by (A17), (A32), and (A35) in appendix A; FRV and FSV are expressed by (A24) and (A41), respectively. They are complicated functions of the fall speeds of rain and snow, which are themselves dependent on q_r and q_s. To make the numerical integration more manageable, we hold these coefficients constant over a microphysics time step so that collection processes (PRACW, PSACI, and PSACW) may be written as

$$\frac{dq_y}{dt} = -\frac{dq_x}{dt} = \mathrm{FXY}\,q_x q_y, \quad (15)$$

and evaporation of rain and snow (PREVP, PSEVP) may be expressed as

$$\frac{dq_v}{dt} = -\frac{dq_y}{dt} = (S - 1)\mathrm{FYV}\,q_y. \quad (16)$$

Here x can be replaced by the subscripts c and i, and y can be replaced by the subscripts r and s, respectively. Term S is equal to S_w, S_m, or S_i, depending on the cloud phase.

A flow chart of the computational procedure is given in Fig. 2. The detrained cloud water and cloud ice are first added to q_c and q_i. Melting and freezing are assumed to be instantaneous. Finite rate processes are assumed to occur simultaneously (time-differenced implicitly) after the corrections to q_c, q_r, q_i, q_s, and T due to melting and freezing processes have been applied. The precipitation of rain and snow is computed last.

Using a finite-difference scheme in time, and introducing the indices (n) and ($n + 1$) to denote successive time levels, (7)–(12) may be approximated as follows:

$$\frac{q_v^{n+1} - q_v^n}{\Delta t} = -\delta_1\gamma_1\left[\frac{q_v^{n+1} - q_{sw}^{n-1}}{\tau_w} + (S_w^{n+1} - 1)\,\mathrm{FRV}\,q_r^n\right] - \delta_1\gamma_2\left[\frac{q_v^{n+1} - q_{sm}^{n+1}}{\tau_m} + (S_m^{n+1} - 1)\,\mathrm{FSV}\,q_s^n\right]$$
$$- \delta_1\gamma_3\left[\frac{q_v^{n+1} - q_{si}^{n-1}}{\tau_i} + (S_i^{n+1} - 1)\,\mathrm{FSV}\,q_s^n\right] - \delta_2\gamma_1\left[\frac{(S_w^n - 1)}{\tau_w} q_c^{n+1} + (S_w^n - 1)\,\mathrm{FRV}\,q_r^{n+1}\right]$$

$$-\delta_2\gamma_2\left[\frac{(S_m^n-1)}{\tau_m}(q_c^{n+1}+q_i^{n+1})+(S_m^n-1)\,\mathrm{FSV}\,q_s^{n+1}\right]$$

$$-\delta_2\gamma_3\left[\frac{(S_i^n-1)}{\tau_i}q_i^{n+1}+(S_i^n-1)\,\mathrm{FSV}\,q_s^{n+1}\right], \tag{17}$$

$$\frac{q_c^{n+1}-q_c^n}{\Delta t}=\delta_1\left[\gamma_1\frac{q_v^{n+1}-q_{sw}^{n+1}}{\tau_w}+\gamma_2\omega\frac{q_v^{n+1}-q_{sm}^{n+1}}{\tau_m}\right]$$

$$+\delta_2\left[\gamma_1\frac{S_w^n-1}{\tau_w}q_c^{n+1}+\gamma_2\omega\frac{S_m^n-1}{\tau_m}(q_c^{n+1}+q_i^{n+1})\right]$$

$$-\gamma_1\alpha(q_c^{n+1}-q_{c0})-\gamma_1\,\mathrm{FCR}\,q_r^nq_c^{n+1}-\gamma_2\,\mathrm{FCS}\,q_s^nq_c^{n+1}, \tag{18}$$

$$\frac{q_r^{n+1}-q_r^n}{\Delta t}=\delta_1\gamma_1(S_w^{n+1}-1)\,\mathrm{FRV}\,q_r^n-\delta_2\gamma_1(S_w^n-1)\,\mathrm{FRV}\,q_r^{n+1}+\gamma_1\alpha(q_c-q_{c0})+\gamma_1\,\mathrm{FCR}\,q_r^nq_c^{n+1}, \tag{19}$$

$$\frac{q_i^{n+1}-q_i^n}{\Delta t}=\delta_1\left[\gamma_2(1-\omega)\frac{q_v^{n+1}-q_{sm}^{n+1}}{\tau_m}+\gamma_3\frac{q_v^{n+1}-q_{si}^{n+1}}{\tau_i}\right]$$

$$+\delta_2\left[\gamma_2(1-\omega)\frac{S_m^n-1}{\tau_m}(q_c^{n+1}+q_i^{n+1})+\gamma_3\frac{S_i^n-1}{\tau_i}q_i^{n+1}\right]$$

$$-(\gamma_2+\gamma_3)\beta(q_i^{n+1}-q_{i0})-(\gamma_2+\gamma_3)\,\mathrm{FIS}\,q_s^nq_i^{n+1} \tag{20}$$

$$\frac{q_s^{n+1}-q_s^n}{\Delta t}=\delta_1[\gamma_2(S_{sm}^{n+1}-1)\,\mathrm{FSV}\;q_s^n+\gamma_3(S_i^{n+1}-1)\,\mathrm{FSV}\,q_s^n]$$

$$-\delta_2[\gamma_2(S_{sm}^n-1)\,\mathrm{FSV}\,q_s^{n+1}+\gamma_3(S_i^n-1)\,\mathrm{FSV}\,q_s^{n+1}]$$

$$+(\gamma_2+\gamma_3)\beta(q_i-q_{i0})+\gamma_2\,\mathrm{FCS}\,q_s^nq_c^{n+1}+(\gamma_2+\gamma_3)\,\mathrm{FIS}\,q_s^nq_i^{n+1}, \tag{21}$$

$$\frac{T^{n+1}-T^n}{\Delta t}=\delta_1\gamma_1\frac{L_c}{c_p}\left[\frac{q_v^{n+1}-q_{sw}^{n+1}}{\tau_w}+(S_w^{n+1}-1)\,\mathrm{FRV}\,q_r^n\right]+\delta_1\gamma_2\frac{L_m}{c_p}\left[\frac{q_v^{n+1}-q_{sm}^{n+1}}{\tau_m}+(S_{sm}^{n+1}-1)\,\mathrm{FSV}\,q_s^n\right]$$

$$+\delta_1\gamma_3\frac{L_s}{c_p}\left[\frac{q_v^{n+1}-q_{si}^n}{\tau_i}+(S_i^{n+1}-1)\,\mathrm{FSV}\,q_s^n\right]+\delta_2\gamma_1\frac{L_c}{c_p}\left[\frac{S_w^n-1}{\tau_w}q_c^{n+1}+(S_w^n-1)\,\mathrm{FRV}\,q_r^{n+1}\right]$$

$$+\delta_2\gamma_2\frac{L_m}{c_p}\left[\frac{S_m^n-1}{\tau_m}q_i^{n+1}+(S_m^n-1)\,\mathrm{FSV}\,q_s^{n+1}\right]$$

$$+\delta_2\gamma_3\frac{L_s}{c_p}\left[\frac{S_i^n-1}{\tau_i}q_i^{n+1}+(S_i^n-1)\,\mathrm{FSV}\,q_s^{n+1}\right]+\gamma_2\frac{L_f}{c_p}\,\mathrm{FCS}\,q_s^nq_c^{n+1}. \tag{22}$$

In (17)–(22) we use

$$S_x^{n+1}=\frac{q_v^{n+1}-q_{sx}^{n+1}}{q_{sx}^{n+1}}\approx\frac{q_v^{n-1}-q_{sx}^{n+1}}{q_{sx}^n}, \tag{23}$$

and

$$q_{sx}^{n+1}=q_{sx}^n+\left(\frac{\partial q_{sx}}{\partial T}\right)^n(T^{n+1}-T^n). \tag{24}$$

Here x can be replaced by the subscripts w, i, or m, depending on the cloud phase.

Equations (17)–(22) may be rearranged to obtain the following matrix equation with the six unknowns q_v^{n+1}, q_c^{n+1}, q_r^{n+1}, q_i^{n+1}, q_s^{n+1}, and T:

$$\begin{bmatrix} M_{vv} & M_{vc} & M_{vr} & M_{vi} & M_{vs} & M_{vT} \\ M_{cv} & M_{cc} & M_{cr} & M_{ci} & M_{cs} & M_{cT} \\ M_{rv} & M_{rc} & M_{rr} & M_{ri} & M_{rs} & M_{rT} \\ M_{iv} & M_{ic} & M_{ir} & M_{ii} & M_{is} & M_{iT} \\ M_{sv} & M_{sc} & M_{sr} & M_{si} & M_{ss} & M_{sT} \\ M_{Tv} & M_{Tc} & M_{Tr} & M_{Ti} & M_{Ts} & M_{TT} \end{bmatrix} \times \begin{bmatrix} q_v^{n+1} \\ q_c^{n+1} \\ q_r^{n+1} \\ q_i^{n+1} \\ q_s^{n+1} \\ T^{n+1} \end{bmatrix} = \begin{bmatrix} C_v \\ C_c \\ C_r \\ C_i \\ C_s \\ C_T \end{bmatrix} \quad (25)$$

Table 3 gives the coefficients M_{xx} and C_x (here x refers to v, c, r, i, s, and T). The system of equations is solved separately for water, ice, and mixed-phase clouds. For single-phase clouds, the system reduces to four equations with the four unknowns q_v, q_c, q_r, and T for the water phase, as given by (26)–(29), and q_v, q_i, q_s, and T for the ice phase. For mixed-phase clouds, the system reduces to five equations with the five unknowns q_v, q_c, q_i, q_s, and T. We choose an implicit technique to solve the time rates of change of the five water species and temperature so that the different microphysical processes may be treated at once instead of sequentially as an explicit scheme would have forced us to do. In doing so, we also avoid problems of overdepletion and the occurrence of negative values of q_c, q_i, q_r, and q_s. The equations for the water phase are as follows ($\gamma_1 = 1$, $\gamma_2 = \gamma_3 = 0$):

$$\left[1 + \delta_1\left(\frac{1}{\tau_w} + \frac{q_r^n}{q_{sw}^n}\,\mathrm{FRV}\right)\Delta t\right] q_v^{n+1} + \frac{\delta_2}{\tau_w}(S_w^n - 1)\Delta t q_c^{n+1} + \delta_2(S_w^n - 1)\,\mathrm{FRV}\,\Delta t q_r^{n+1}$$
$$- \delta_1\left[\frac{1}{\tau_w} + \frac{q_r^n}{q_{sw}^n}\,\mathrm{FRV}\right]\left(\frac{\partial q_{sw}}{\partial T}\right)^n \Delta t T^{n+1} = q_v^n + \delta_1\left[\frac{1}{\tau_w} + \frac{q_r^n}{q_{sw}^n}\,\mathrm{FRV}\right]\left(q_{sw}^n - \left(\frac{\partial q_{sw}}{\partial T}\right)^n T^n\right)\Delta t \quad (26)$$

$$-\frac{\delta_1}{\tau_w}\Delta t q_v^{n+1} + \left[1 - \left(\delta_2\frac{S_w^n - 1}{\tau_w} - \alpha - \mathrm{FCR}\,q_r^n\right)\Delta t\right] q_c^{n+1}$$
$$+ \frac{\delta_1}{\tau_w}\left(\frac{\partial q_{sw}}{\partial T}\right)^n \Delta t T^{n+1} = q_c^n + \left[\alpha q_{c0} - \frac{\delta_1}{\tau_w}\left(q_{sw}^n - \left(\frac{\partial q_{sw}}{\partial T}\right)^n T^n\right)\right]\Delta t \quad (27)$$

$$-\delta_1\frac{q_r^n}{q_{sw}^n}\,\mathrm{FRV}\,\Delta t q_v^{n+1} - [\alpha + \mathrm{FCR}\,q_r^n]\Delta t q_c^{n+1} + [1 - \delta_2(S_w^n - 1)\,\mathrm{FRV}\,\Delta t] q_r^{n+1}$$
$$+ \delta_1\frac{q_r^n}{q_{sw}^n}\,\mathrm{FRV}\left(\frac{\partial q_{sw}}{\partial T}\right)^n \Delta t T^{n+1} = q_r^n - \left(\alpha q_{c0} + \delta_1\frac{q_r^n}{q_{sw}^n}\,\mathrm{FRV}\left(q_{sw}^n - \left(\frac{\partial q_{sw}}{\partial T}\right)^n T^n\right)\right)\Delta t \quad (28)$$

$$-\delta_1\frac{L_c}{c_p}\left(\frac{1}{\tau_w} + \frac{q_r^n}{q_{sw}^n}\,\mathrm{FRV}\right)\Delta t q_v^{n+1} - \delta_2\frac{L_c}{c_p}\frac{S_w^n - 1}{\tau_w}\Delta t q_c^{n+1} - \delta_2\frac{L_c}{c_p}(S_w^n - 1)\,\mathrm{FRV}\,\Delta t q_r^{n+1}$$
$$+ \left[1 + \delta_1\frac{L_c}{c_p}\left(\frac{1}{\tau_w} + \frac{q_r^n}{q_{sw}^n}\,\mathrm{FRV}\right)\left(\frac{\partial q_{sw}}{\partial T}\right)^n \Delta t\right] T^{n+1}$$
$$= T^n - \delta_1\frac{L_c}{c_p}\left(\frac{1}{\tau_w} + \frac{q_r^n}{q_{sw}^n}\,\mathrm{FRV}\right)\left[q_{sw}^n - \left(\frac{\partial q_{sw}}{\partial T}\right)^n T^n\right]\Delta t. \quad (29)$$

Similar sets of equations may be derived for the ice and mixed phases using the coefficients listed in Table 3. They are omitted here for brevity.

The cloud microphysics scheme is applied to model layers located above the PBL, up to 100 mb. We have chosen not to include PBL clouds in the framework of our microphysics parameterization at this time. The reason is that we are in the midst of a complete overhaul of our boundary-layer parameterization, not only changing the boundary-layer clouds but also eliminating the mixed-layer assumption (Randall et al. 1992) and revising the entrainment parameterization. We have therefore decided to revise the boundary-layer clouds as part of "Phase 2" of the development of our

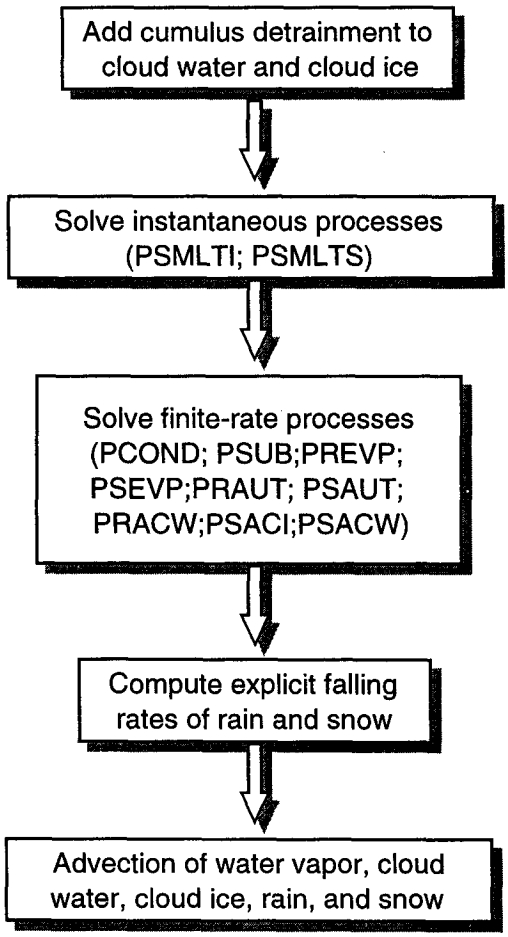

FIG. 2. Flow chart of computational procedure of the cloud microphysics scheme.

cloud microphysics parameterization. This will be reported at a later time.

Cloud water, cloud ice, rain, and snow are advected using a fourth-order advection scheme. With the current model's coarse resolution, advective processes have a small effect on the global distributions of the moisture budget components, but they must be included to ensure conservation of total water mass. In higher-resolution models these terms will become important.

b. *Bergeron–Findeisen mechanism*

The Bergeron–Findeisen mechanism (Bergeron 1935) is the microphysical process that describes the growth of cloud ice at the expense of cloud water, and the enhanced precipitation due to collection of cloud water by snow when cloud ice, cloud water, and snow coexist in a cloud. This mechanism exists because the saturation vapor pressure with respect to ice (e_{si}) is less than that with respect to water (e_{sw}). It is most effective at about −12°C, where the difference between e_{sw} and e_{si} is the largest. In mixed-phase clouds, the partitioning of the total condensate between cloud water and cloud ice, under control of the microphysics process PBERG, is formulated as a function of temperature. The Bergeron–Findeisen process is parameterized through two different mechanisms: 1) increased amounts of cloud ice are produced at the expense of supercooled water when the temperature is low enough and 2) enhanced conversion to precipitation is parameterized by the microphysical process PSACW. Both mechanisms act to reduce the amount of supercooled water in the cloud.

Our particular treatment of the Bergeron–Findeisen mechanism was designed so that we can use the implicit scheme described above to compute the time rates of change for the supercooled cloud water and cloud ice mixing ratios in mixed-phase clouds. The saturation vapor pressure e_{sm} for temperatures between T_{00} and T_0, is obtained by linear interpolation between the saturation vapor pressures with respect to water and ice:

$$e_{sm}(T) = \omega e_{sw}(T) + (1 - \omega) e_{si}(T). \quad (30)$$

Here the weight (ω) is defined as

$$\omega = \frac{T - T_{00}}{T_0 - T_{00}} \quad (31)$$

so that $\omega = 0$ for $T = T_{00}$ and $\omega = 1$ for $T = T_0$. The saturation S_m and the saturation mixing ratio q_{sm} are then computed using $e_{sm}(T)$. Equations (30)–(31) allow us to describe deposition and sublimation processes for the mixed phase with expressions similar to those used for the water and ice phases [see (A11)–(A12) and (A25)–(A26)]. The partitioning between q_c and q_i is then obtained by assuming that

$$\frac{\partial q_c}{\partial t} = \omega \frac{\partial}{\partial t}(q_c + q_i) \quad \text{and}$$

$$\frac{\partial q_i}{\partial t} = (1 - \omega) \frac{\partial}{\partial t}(q_c + q_i). \quad (32)$$

This allows conservation of the generalized moist static energy, as explained in appendix A.

c. *Precipitation processes*

We have chosen to explicitly time step the precipitation process for rain and snow using a small time step (two minutes) with a time-splitting method. This choice may seem odd in view of the rapid fall speeds of rain and snow particles. Considering that for a fall speed of 5 m s^{-1} a particle can fall through the depth of the troposphere in about 2000–3000 sec, the assumption of instantaneous removal may seem more appropriate. Our reason for not assuming instantaneous removal and for time stepping the precipitation process instead is that precipitation particles are subject to various microphysical processes as they fall. Rain and

TABLE 3. Coefficients of the matrix equation that solves the implicit sheme of the bulk cloud microphysics parameterization.

Element	Coefficient
	Water vapor
M_{vv}	$1 + \delta_1\left[\gamma_1\left(\frac{1}{\tau_w} + \frac{q_r^n}{q_{sw}^n}\,\mathrm{FRV}\right) + \gamma_2\left(\frac{1}{\tau_m} + \frac{q_s^n}{q_{sm}^n}\,\mathrm{FSV}\right) + \gamma_3\left(\frac{1}{\tau_i} + \frac{q_s^n}{q_{si}^n}\,\mathrm{FSV}\right)\right]\Delta t$
M_{vc}	$\delta_2\left[\gamma_1\frac{S_w^n - 1}{\tau_w} + \gamma_2\frac{S_m^n - 1}{\tau_m}\right]\Delta t$
M_{vr}	$\delta_2\gamma_1(S_w^n - 1)\,\mathrm{FRV}\,\Delta t$
M_{vi}	$\delta_2\left[\gamma_2\frac{S_m^n - 1}{\tau_m} + \gamma_3\frac{S_{si}^n - 1}{\tau_i}\right]\Delta t$
M_{vs}	$\delta_2[\gamma_2(S_m^n - 1)\,\mathrm{FSV} + \gamma_3(S_i^n - 1)\,\mathrm{FSV}]\Delta t$
M_{vT}	$-\delta_1\left[\gamma_1\left(\frac{1}{\tau_w} + \frac{q_r^n}{q_{sw}^n}\,\mathrm{FRV}\right)\left(\frac{\partial q_{sw}}{\partial T}\right)^n + \gamma_2\left(\frac{1}{\tau_m} + \frac{q_s^n}{q_{sm}^n}\,\mathrm{FSV}\right)\left(\frac{\partial q_{sm}}{\partial T}\right)^n + \gamma_3\left(\frac{1}{\tau_i} + \frac{q_s^n}{q_{si}^n}\,\mathrm{FSV}\right)\left(\frac{\partial q_{si}}{\partial T}\right)^n\right]\Delta t$
C_v	$q_v^n + \delta_1\left(\gamma_1\left[\frac{1}{\tau_w} + \frac{q_r^n}{q_{sw}^n}\,\mathrm{FRV}\right]\left(q_{sw}^n - \left(\frac{\partial q_{sw}}{\partial T}\right)^n T^n\right) + \gamma_2\left[\frac{1}{\tau_m} + \frac{q_s^n}{q_{sm}^n}\,\mathrm{FSV}\right]\left(q_{sm}^n - \left(\frac{\partial q_{sm}}{\partial T}\right)^n T^n\right)\right) + \gamma_3\left[\frac{1}{\tau_i} + \frac{q_s^n}{q_{si}^n}\,\mathrm{FSV}\right]$ $\times\left(q_{si}^n - \left(\frac{\partial q_{si}}{\partial T}\right)^n T^n\right)\Delta t$
	Cloud water
M_{cv}	$-\delta_1\left(\gamma_1\frac{1}{\tau_w} + \gamma_2\omega\frac{1}{\tau_m}\right)\Delta t$
M_{cc}	$1 - \left[\delta_2\left(\gamma_1\frac{S_w^n - 1}{\tau_w} + \gamma_2\omega\frac{S_m^n - 1}{\tau_m}\right) - \gamma_1\alpha - \gamma_1\mathrm{FRC}\,q_r^n - \gamma_2\mathrm{FCS}\,q_s^n\right]\Delta t$
M_{cr}	0
M_{ci}	0
M_{cs}	0
M_{cT}	$\delta_1\left(\gamma_1\frac{1}{\tau_w}\left(\frac{\partial q_{sw}}{\partial T}\right)^n + \gamma_2\omega\frac{1}{\tau_m}\left(\frac{\partial q_{sm}}{\partial T}\right)^n\right)\Delta t$
C_c	$q_c^n + \left(\gamma_1\,\alpha q_{c0} - \gamma_1\frac{\delta_1}{\tau_w}\left(q_{sw}^n - \left(\frac{\partial q_{sw}}{\partial T}\right)^n T^n\right) - \gamma_2\omega\frac{\delta_1}{\tau_m}\left(q_{sm}^n - \left(\frac{\partial q_{sm}}{\partial T}\right)^n T^n\right)\right)\Delta t$
	Rain
M_{rv}	$-\delta_1\,\gamma_1\frac{q_r^n}{q_{sw}^n}\,\mathrm{FRV}\,\Delta t$
M_{rc}	$-\gamma_1(\alpha + \mathrm{FCR}\,q_r^n)\Delta t$
M_{rr}	$1 - \delta_2\gamma_1\,(S_w^n - 1)\mathrm{FRV}\Delta t$
M_{ri}	0
M_{rs}	0
M_{rT}	$\delta_1\,\gamma_1\frac{q_r^n}{q_{sw}^n}\,\mathrm{FRV}\left(\frac{\partial q_{sw}}{\partial T}\right)^n\Delta t$
C_r	$q_r^n - \gamma_1\left(\alpha q_{c0} + \delta_1\frac{q_r^n}{q_{sw}^n}\,\mathrm{FRV}\left(q_{sw}^n - \left(\frac{\partial q_{sw}}{\partial T}\right)^n T^n\right)\right)\Delta t$

TABLE 3. (*Continued*)

Element	Coefficient
	Cloud ice
M_{iv}	$-\delta_1\left(\gamma_2 (1-\omega)\frac{1}{\tau_m} + \gamma_3 \frac{1}{\tau_i}\right)\Delta t$
M_{ic}	0
M_{ir}	0
M_{ii}	$1 - \left[\delta_2\left(\gamma_2 (1-\omega)\frac{S_m^n - 1}{\tau_m} + \gamma_3 \frac{S_i^n - 1}{\tau_i}\right) - (\gamma_2 + \gamma_3)\beta - (\gamma_2 + \gamma_3)\,\mathrm{FIS}\, q_s^n\right]\Delta t$
M_{is}	0
M_{iT}	$\delta_1\left(\gamma_2 (1-\omega)\frac{1}{\tau_m}\left(\frac{\partial q_{sm}}{\partial T}\right)^n + \gamma_3 \frac{1}{\tau_i}\left(\frac{\partial q_{si}}{\partial T}\right)^n\right)\Delta t$
C_i	$q_i^n + \left((\gamma_2 + \gamma_3)\beta q_{i0} - \gamma_2 \frac{\delta_1}{\tau_m}(1-\omega)\left(q_{sm}^n - \left(\frac{\partial q_{sm}}{\partial T}\right)^n T^n\right) - \gamma_3 \frac{\delta_1}{\tau_i}\left(q_{si}^n - \left(\frac{\partial q_{si}}{\partial T}\right)^n T^n\right)\right)\Delta t$
	Snow
M_{sv}	$-\delta_1\left[\gamma_2 \frac{q_s^n}{q_{sm}^n} + \gamma_3 \frac{q_s^n}{q_{si}^n}\right]\mathrm{FSV}\,\Delta t$
M_{sc}	$-\gamma_2\,\mathrm{FSC}\, q_s^n \Delta t$
M_{sr}	0
M_{si}	$-(\gamma_2 + \gamma_3)\,(\beta + \mathrm{FIS}\, q_s^n)\Delta t$
M_{ss}	$1 - \delta_2\,[\gamma_2(S_m^n - 1)\,\mathrm{FSV} + \gamma_3\,(S_i^n - 1)\,\mathrm{FSV}]\Delta t$
M_{sT}	$\delta_1\left[\gamma_2 \frac{q_s^n}{q_{sm}^n}\,\mathrm{FSV}\left(\frac{\partial q_{sm}}{\partial T}\right)^n + \gamma_3 \frac{q_s^n}{q_{si}^n}\,\mathrm{FSV}\left(\frac{\partial q_{si}}{\partial T}\right)^n\right]\Delta t$
C_s	$q_s^n - \left[(\gamma_2 + \gamma_3)\beta q_{i0} + \delta_1\gamma_2 \frac{q_s^n}{q_{sm}^n}\,\mathrm{FSV}\left(q_{sm}^n - \left(\frac{\partial q_{sm}}{\partial T}\right)^n T^n\right) + \delta_1\gamma_3 \frac{q_s^n}{q_{si}^n}\,\mathrm{FSV}\left(q_{si}^n - \left(\frac{\partial q_{si}}{\partial T}\right)^n T^n\right)\right]\Delta t$
	Temperature
M_{Tv}	$-\delta_1\left[\gamma_1 \frac{L_v}{c_p}\left(\frac{1}{\tau_w} + \frac{q_r^n}{q_{sw}^n}\,\mathrm{FRV}\right) + \gamma_2\left(\frac{L_m}{c_p}\frac{1}{\tau_m} + \frac{L_s}{c_p}\frac{q_s^n}{q_{sm}^n}\,\mathrm{FSV}\right) + \gamma_3 \frac{L_s}{c_p}\left(\frac{1}{\tau_i} + \frac{q_s^n}{q_{si}^n}\,\mathrm{FSV}\right)\right]\Delta t$
M_{Tc}	$-\delta_2\left[\gamma_1 \frac{L_v}{c_p}\frac{S_w^n - 1}{\tau_w} + \gamma_2 \frac{L_m}{c_p}\frac{S_m^n - 1}{\tau_m}\right]\Delta t - \gamma_2 \frac{L_f}{c_p}\,\mathrm{FCS}\, q_s^n \Delta t$
M_{Tr}	$-\delta_2\,\gamma_1 \frac{L_v}{c_p}(S_w^n - 1)\,\mathrm{FRV}\,\Delta t$
M_{Ti}	$-\delta_2\left[\gamma_2 \frac{L_m}{c_p}\frac{S_m^n - 1}{\tau_m} + \gamma_3 \frac{L_s}{c_p}\frac{S_i^n - 1}{\tau_i}\right]\Delta t$
M_{Ts}	$-\delta_2\left[\gamma_2 \frac{L_s}{c_p}(S_m^n - 1)\,\mathrm{FSV}\,\Delta t + \gamma_3 \frac{L_s}{c_p}(S_i^n - 1)\,\mathrm{FSV}\,\Delta t\right]$
M_{TT}	$1 + \delta_1\gamma_1 \frac{L_v}{c_p}\left[\left(\frac{1}{\tau_w} + \frac{q_r^n}{q_{sw}^n}\,\mathrm{FRV}\right)\left(\frac{\partial q_{sw}}{\partial T}\right)^n\right]\Delta t + \delta_1\gamma_2\left(\frac{L_m}{c_p}\frac{1}{\tau_m} + \frac{L_s}{c_p}\frac{q_s^n}{q_{sm}^n}\,\mathrm{FSV}\right)\left(\frac{\partial q_{sm}}{\partial T}\right)^n \Delta t$
	$+ \delta_1\,\gamma_3 \frac{L_s}{c_p}\left[\left(\frac{1}{\tau_i} + \frac{q_s^n}{q_{si}^n}\,\mathrm{FSV}\right)\left(\frac{\partial q_{si}}{\partial T}\right)^n\right]\Delta t$
C_T	$T^n - \delta_1\gamma_1 \frac{L_v}{c_p}\left[\left(\frac{1}{\tau_w} + \frac{q_r^n}{q_{sw}^n}\,\mathrm{FRV}\right)\left(q_{sw}^n - \left(\frac{\partial q_{sw}}{\partial T}\right)^n T^n\right)\right]\Delta t - \delta_1\gamma_2\left(\frac{L_m}{c_p}\frac{1}{\tau_m} + \frac{L_s}{c_p}\frac{q_s^n}{q_{sm}^n}\,\mathrm{FSV}\right)\left(q_{sm}^n - \left(\frac{\partial q_{sm}}{\partial T}\right)^n T^n\right)\Delta t$
	$- \delta_1\gamma_3 \frac{L_s}{c_p}\left[\left(\frac{1}{\tau_i} + \frac{q_s^n}{q_{si}^n}\,\mathrm{FSV}\right)\left(q_{si}^n - \left(\frac{\partial q_{si}}{\partial T}\right)^n T^n\right)\right]\Delta t$

snow may evaporate, collect other particles, freeze or melt, etc. By far the simplest and most rigorous way to take these processes into account is to time step the precipitation.

We express the tendency of rain or snow due to precipitation, that is, the rate of change of the rain (snow) mixing ratio while rain (snow) is falling through the atmosphere (P_x in kg kg^{-1} s^{-1}, where x refers to the subscripts r for rain and s for snow) by

$$P_x = g \frac{d}{dp} (\rho q_x V_x), \tag{33}$$

where g is the gravitational acceleration, ρ is the air density, q_x is the mixing ratio, and V_x is the fallspeed.

d. *Cloud amount and scale dependence of microphysical parameters*

Like the UCLA model from which it was derived, the CSU model does not currently include a parameterization of fractional cloudiness for stratiform clouds above the boundary layer. We are developing one at this time (Randall 1987; Xu and Randall 1994), but in the model and results described here the cloud amount is assumed to be 100% when $q_c + q_i + q_s \geq 10^{-5}$ kg kg^{-1} in any grid cell and zero, otherwise. Since the optical thickness and emittance of clouds are functions of the condensed water (see Part II), they vary continuously as cloud form and dissipate.

Nevertheless, a parameterization of cloud amount is urgently needed for two reasons. First, and most obviously, it is needed for the radiative transfer calculations (Harshvardhan and Randall 1985). Of equal importance, however, is the role of cloud amount in the microphysics parameterization. The parameterization presented in this paper is primarily based on one developed by Rutledge and Hobbs (1983) and Lin et al. (1983) for use in a mesoscale model, and the condensed water mixing ratios used are supposed to represent local in-cloud values. When the parameterization is applied in a large-scale model in which grid cells may often be partly cloudy, the condensed water mixing ratios predicted by the model represent averages over both the cloudy and clear portions of a grid cell. Such averages can be much smaller than the local in-cloud values required by the microphysics parameterization. If the cloud amount is known, then in-cloud condensate mixing ratios can be estimated by dividing the corresponding grid-cell mean mixing ratios by the cloud amount. Because the cloud amount is not known in the present version of our model, we cannot do this.

Instead, we are forced to make arbitrary changes in some of the microphysical parameters used. In particular, we have reduced the autoconversion thresholds to values drastically smaller than those recommended by Rutledge and Hobbs (1983) and Lin et al. (1983). For autoconversion of cloud water to rain, we use 0.25 $\times 10^{-3}$ kg kg^{-1} instead of 0.7 $\times 10^{-3}$ kg kg^{-1}, which was recommended by Rutledge and Hobbs (1983). For autoconversion of cloud ice to snow, we use 0.01 $\times 10^{-3}$ kg kg^{-1} instead of 0.1 $\times 10^{-3}$ kg kg^{-1}, which was recommended by Lin et al. (1983). Fowler and Randall (1994) discuss the sensitivity of the model results to these choices.

In the near future, when we test a cloud amount parameterization in the GCM, we will be able to increase the autoconversion coefficients to more conventional values. The degree to which we can use the thresholds recommended by Rutledge and Hobbs (1983) and Lin et al. (1983) will be one measure of the success of our cloud amount parameterization.

e. *Interactions with cumulus convection*

Stratiform clouds are coupled with convection through detrainment of cloud water and cloud ice from the tops of cumulus towers. This coupling leads to the formation of horizontally extensive upper-tropospheric anvil clouds and cirrus debris arising from deep convective activity. The parameterization of moist convection originating in the planetary boundary layer (PBL) consists of a modified version of the Arakawa–Schubert scheme (1974; see also Lord 1982 and Lord et al. 1982). A key feature of this modified Arakawa–Schubert parameterization is that it includes a prognostic cumulus kinetic energy, as described by Randall and Pan (1993). Cumulus updrafts are assumed to originate only in the PBL and to transport mass upward in the free troposphere. The PBL mass is then replenished by turbulent entrainment and large-scale mass convergence. The partitioning of total detrained water between cloud water and cloud ice depends on temperature, following Lord (1982). For $T \geq -10$°C, the condensate is detrained entirely as cloud water. For $T < -40$°C, it is detrained entirely as cloud ice. In the temperature range -40°C $\leq T < -10$°C, the partitioning of detrained condensed water between cloud water and cloud ice depends linearly on temperature. The penetrative convection scheme is supplemented by moist convective adjustment (Manabe et al. 1965) to remove any convective instability in the free troposphere. A dry convective adjustment scheme also mixes water vapor between adjacent layers.

In the formulation of the cumulus parameterization, it is assumed (Arakawa and Schubert 1974) that the fractional area covered by active cumulus updrafts is negligibly small. For this reason, it is not possible, with the current cumulus parameterization, to predict the amount of water and/or ice that is stored inside the cumulus updrafts (the cumulus parameterization is designed for use in large-scale models with grid cells hundreds of kilometers across and certainly is not applicable to higher-resolution models in which the fraction of a grid cell occupied by active cumulus updrafts might be considerably larger). The prognostic cloud microphysical variables of the model represent the con-

densed water in the stratiform clouds outside the cumulus towers, although as mentioned above the liquid water and ice detrained from the cumulus clouds do act as sources for the prognostic microphysical variables. Here we define "stratiform clouds" to be clouds neutrally buoyant with respect to their environment.

3. Computational design

The core of the CSU GCM is based on a version of the UCLA/GCM described in Harshvardhan et al. (1989), Randall et al. (1989), and Randall and Dazlich (1991). Major modifications to the original code include an improved cumulus parameterization (Randall and Pan 1993, described in section 2e), and the inclusion of an updated version of the Simple Biosphere Model (SiB) of Sellers et al. (1986 described by Sellers et al. 1993). The version of the CSU GCM used here is a 17-level gridpoint model with a horizontal resolution of 4° in latitude by 5° in longitude. The vertical discretization is based on a modified σ coordinate in which the planetary boundary layer (PBL) is the bottom layer of the model (Suarez et al. 1983). Details of the parameterization of radiative transfer through clouds are provided in Part II.

There are two important differences between the "EAULIQ" and "CONTROL" runs:

(i) In EAULIQ, the bulk cloud microphysics scheme is used to simulate large-scale condensation processes. In contrast, CONTROL uses a conventional large-scale condensation scheme. CONTROL does not allow for storage of condensed species in the atmosphere. Condensed water is predicted to form and be removed instantaneously from the atmosphere in the form of rain when the large-scale relative humidity exceeds 100%. Ice effects in stratiform clouds are not included. Rain is allowed to evaporate while falling through subsaturated layers. There is no direct coupling between cumulus and large-scale condensation. All moisture detrained from cumulus clouds is assumed to be in the form of water vapor. This means that detrained ice and liquid are converted back to vapor as part of the cumulus parameterization, and as a result the "cumulus heating" is actually negative near the top of the convective layer, as discussed by Randall et al. (1989). Of course, the detrained vapor moistens the environment, and the evaporative chilling also increases the relative humidity near the cumulus cloud tops, so that typically large-scale supersaturation occurs. The large-scale saturation routine then recondenses the vapor, but it produces only liquid, not ice, that is instantaneously removed from the atmosphere in the form of rain, or may also evaporate. This is a disturbing inconsistency in CONTROL that has been eliminated with the introduction of EAULIQ.

(ii) The parameterizations of cloudiness and cloud optical properties have been revised. The results are described in Part II, where differences between EAULIQ and CONTROL in the simulated cloudiness, cloud optical depths, and cloud infrared emissivities are discussed. In EAULIQ, the optical effects of cloud water, cloud ice, and snow are considered; those of rain are neglected because the fall speed of rain is about three times larger than that of snow (about 6 m s^{-1} for rain versus 2 m s^{-1} for snow), and "rain clouds" would then have very short lifetimes. Also, if we assume that the optical thickness is inversely proportional to the effective radius of the water species following Stephens (1978), the optical thickness of rain would be quite small since the effective radius of rain is in the order of several millimeters.

In CONTROL, the cloud optical depth and infrared emissivity are computed as functions of the cloud mean temperature, following the formulation proposed by Harshvardhan et al. (1989).

EAULIQ and CONTROL were both run through a full annual cycle after a three-month spinup. The initial atmospheric states for both runs correspond to 1 October of a prior long-term climate simulation performed without cloud microphysics. In EAULIQ, the initial mixing ratios of cloud water, cloud ice, rain, and snow were set to zero. Sea surface temperatures follow seasonally varying climatology. Full solar and infrared radiative transfer calculations were made every hour to take into account the diurnal variations of radiation and clouds. At present, convection is computed every hour. The dynamics time step is 6 min. The cloud microphysics scheme is embedded in the model dynamics and uses a 2-min time step so that precipitation of rain and snow can be computed explicitly. In section 4, January and July monthly mean results are presented.

4. EAULIQ's hydrologic cycle

a. Convective and microphysical processes

One important characteristic of the Arakawa–Schubert (1974) cumulus parameterization is its ability to predict the rates at which cloud water and cloud ice are detrained at cloud top. Figure 3 shows the latitude–height cross sections of the January-mean detrainment rates for cloud water and cloud ice. The results for July are very similar apart from obvious seasonal shifts, and are omitted here for brevity. The partitioning between the detrained cloud water and cloud ice is a function of temperature, as discussed in section 2e. A comparison of Figs. 3a and 3b shows that the cumulus parameterization detrains more cloud ice than cloud water. This difference in the detrainment rates of the two species affects the partitioning between the large-scale cloud water and cloud ice amounts, as discussed later. Detrainment of cloud water has a maximum at about 8 km, while detrainment of cloud ice is the strongest above 12 km and leads to the formation of upper-tro-

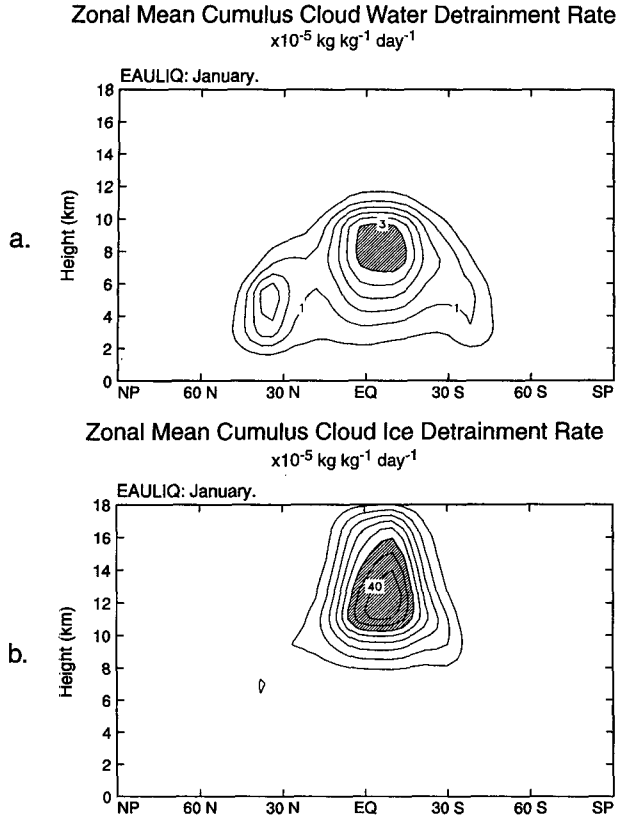

FIG. 3. Latitude–height cross sections of the monthly averaged cumulus detrainment rate of (a) cloud water and (b) cloud ice for January. Units are 10^{-5} kg kg^{-1} day^{-1}. The contour intervals are every 0.5×10^{-5} kg kg^{-1} day^{-1} for (a) and every 5×10^{-5} kg kg^{-1} day^{-1} for (b). Shading corresponds to values greater than 3×10^{-5} kg kg^{-1} day^{-1} for (a) and greater than 30×10^{-5} kg kg^{-1} day^{-1} for (b).

pospheric stratiform clouds and associated cirrus debris.

To illustrate some of the processes included in the cloud microphysics parameterization, we present, in Fig. 4, latitude–height cross sections of the zonally averaged tendencies of rain and snow due to precipitation. Positive and negative values of the tendencies correspond to gains and losses of rain and snow, respectively. As in Fig. 3, only January means are presented. In accordance with the decrease of temperature with latitude, water clouds are predominantly confined between 60°N and 60°S and are replaced by ice clouds at higher latitudes. Following the temperature lapse rate, water clouds dominate in the lower troposphere and are replaced by ice clouds in the upper troposphere. The tendency of rain shows several minima between 40°N and 40°S, all near the 3-km level. It can be shown that the tendency of rain becomes positive below the 1-km level, indicating a gain of rain there. This is not surprising since no cloud microphysics processes are allowed to take place outside of the free troposphere, and rain and snow accumulating at the PBL top are immediately transferred to the surface in the form of precipitation. As seen in Fig. 4b, the tendency of snow is largest near the equator below the tropical tropopause, and in the middle latitudes of the winter hemisphere. A secondary minima is located in the middle latitudes of the summer hemisphere, near the 6 km level. This is in accordance with the autoconversion of cloud ice and collection of cloud ice to form snow, as discussed in the next section. The change in the sign of the tendency of snow occurs along the 0° isotherm, due to the melting of snow to rain below the freezing level.

b. Atmospheric moisture budget

We now examine the monthly mean distributions of the various components of the atmospheric moisture budget except for water vapor (WV). The WV distributions simulated with EAULIQ and CONTROL are discussed in section 5. Figures 5 and 6 show January and July maps of the vertically integrated amounts of cloud water (CW), cloud ice (CI), rain (RW), and

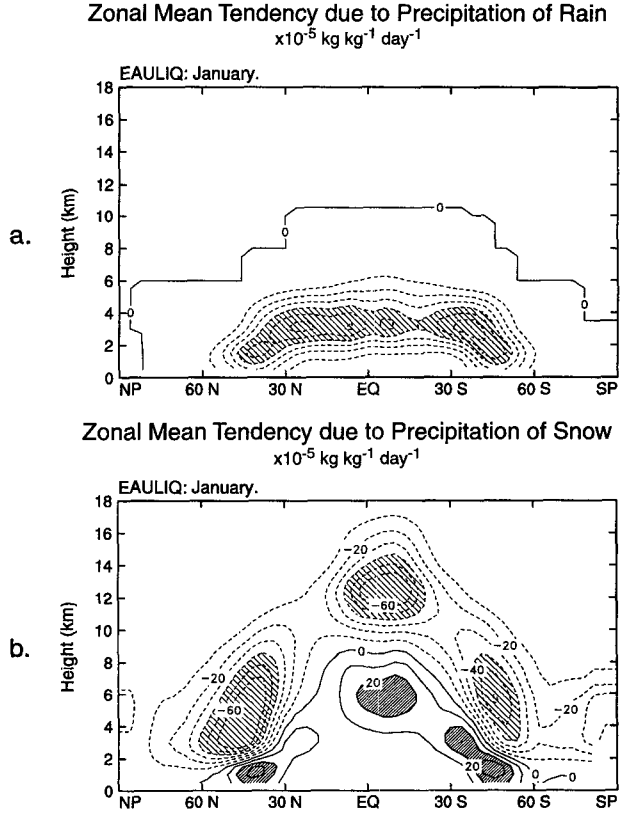

FIG. 4. Latitude–height cross sections of the monthly averaged tendencies due to precipitation for January: (a) tendency of rain and (b) tendency of snow. Units are 10^{-5} kg kg^{-1} day^{-1}, and contour intervals are every 10×10^{-5} kg kg^{-1} day^{-1}. Light shading corresponds to values less than -40×10^{-5} kg kg^{-1} day^{-1} and heavy shading corresponds to values greater than 20×10^{-5} kg kg^{-1} day^{-1}.

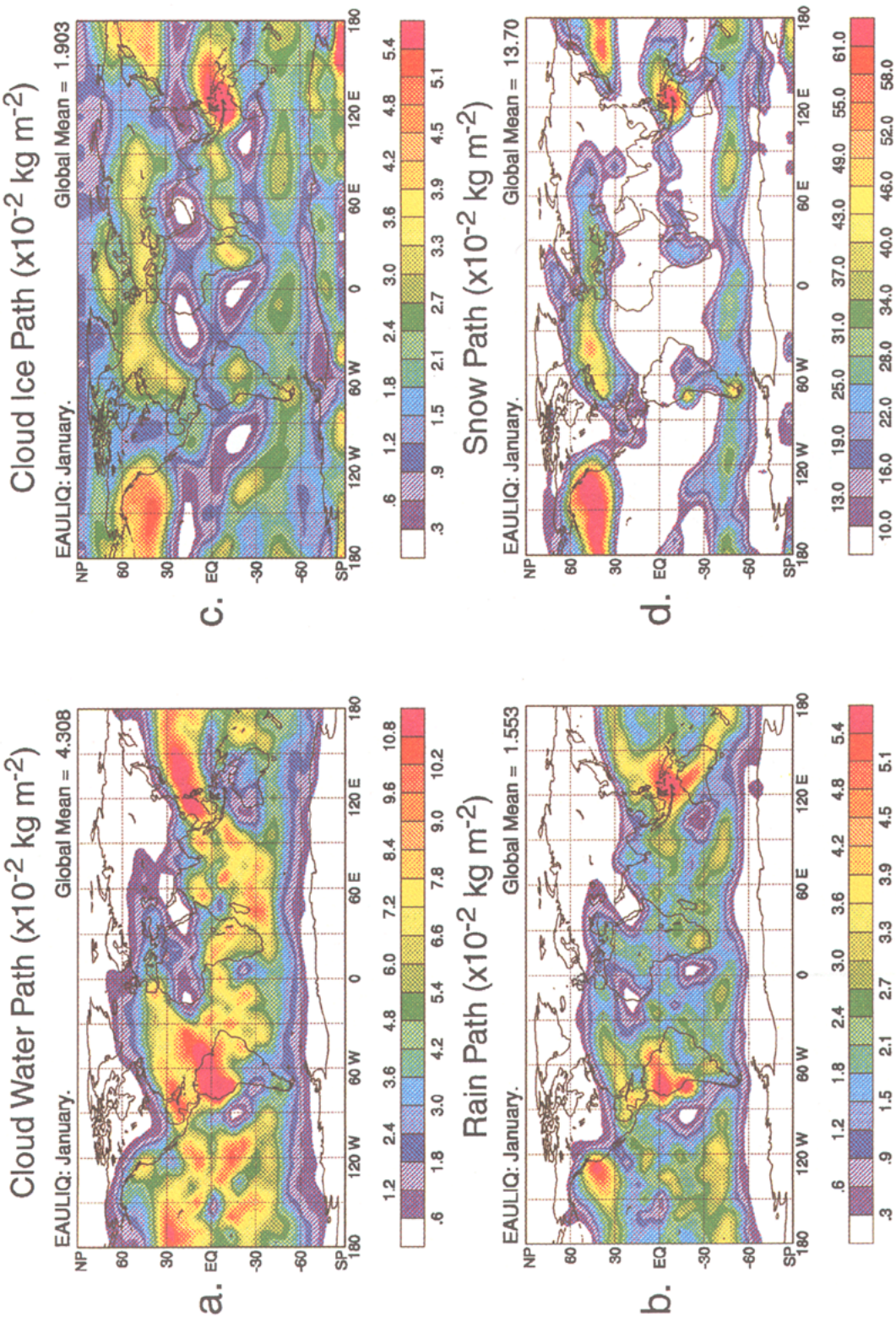

FIG. 5. Global maps of the monthly averaged vertically integrated (a) cloud water, (b) cloud ice, (c) rain, and (d) snow for January. Units are 10^{-2} kg m^{-2}.

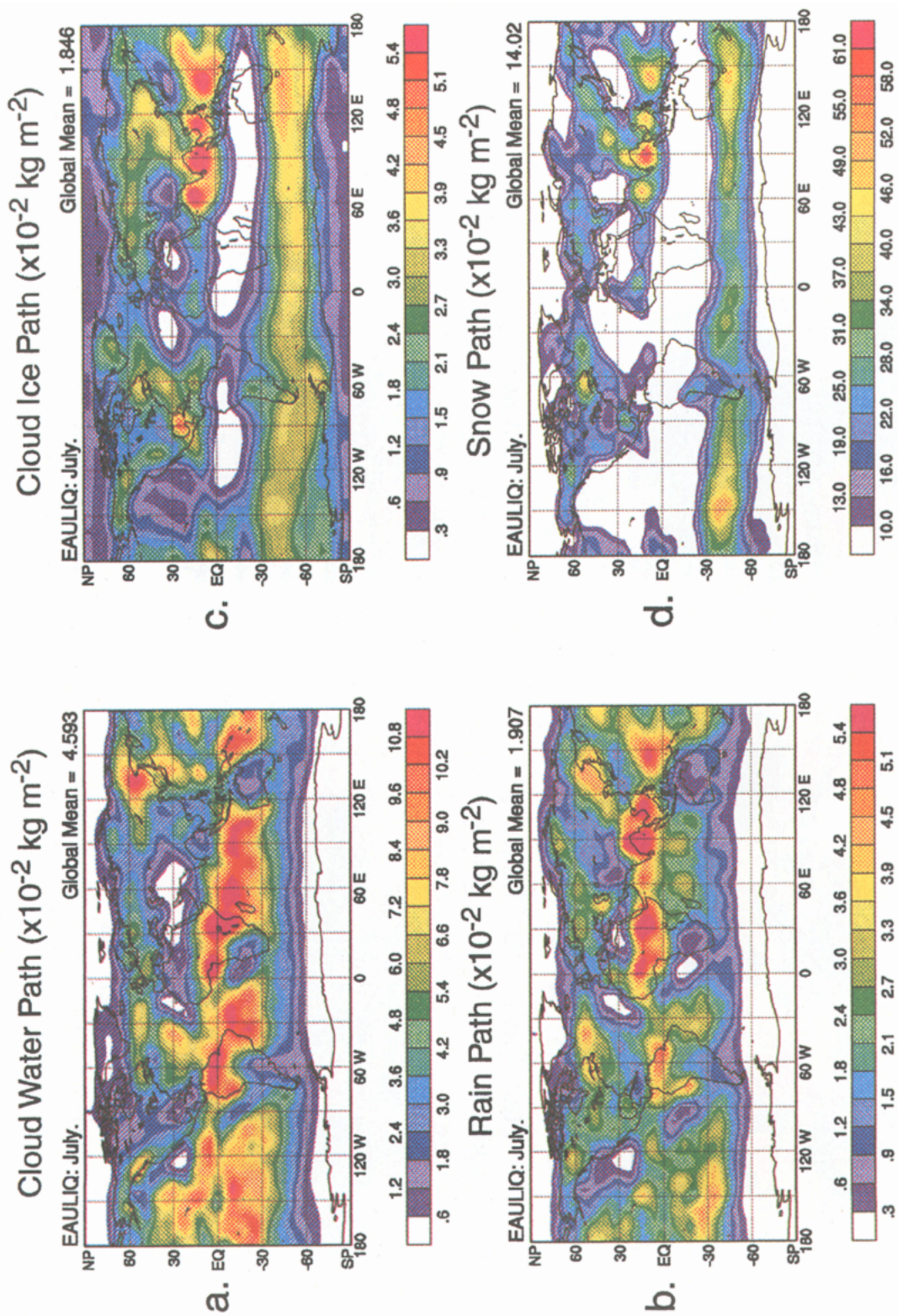

FIG. 6. As Fig. 5 but for July. Units are 10^{-2} kg m^{-2}.

snow (RI) inside the atmosphere. Figures 7 and 8 present latitude–height cross sections of the zonally averaged CW, CI, RW, and RI for January and July, respectively.

Cloud water and cloud ice are detrained at the tops of cumulus towers, primarily over the deep tropical regions of convective activity. They are also produced by large-scale supersaturation, primarily in the Tropics and the middle latitudes. As may be seen in Fig. 5 for January and Fig. 6 for July, maxima of CW and CI are located over the chief tropical convective activity regions in conjunction with strong detrainment of condensed water and over the North Pacific and North Atlantic storm track regions in January and the Southern Ocean in July in conjunction with midlatitude cyclone activity. CW appears to be more abundant in the warm Tropics than in the cool midlatitudes, especially over land, and CW is more abundant than CI in both January and July. On a global average for January, CW is equal to 0.043 kg m^{-2}, whereas CI is equal to 0.019 kg m^{-2}. For July, CW is equal to 0.046 kg m^{-2} and CI is 0.018 kg m^{-2}. Minima of CW and CI are found over the major desert regions and the subtropical oceans.

The vertical distributions of CW and CI are naturally quite different. In January, CW displays a maximum in the lower troposphere in the Tropics located near the 3-km level whereas, in July, CW shows a primary maximum south of the equator and a secondary maximum near 60°N, also near the 3-km level. In contrast, CI shows a primary maximum in the tropical upper troposphere and a secondary maximum in the midlatitudes in the winter hemisphere. In the Tropics, the primary maximum of CI is located at the same altitude than the maximum cloud ice detrainment rate, indicating that CI results predominantly from the detrainment of cloud ice at the tops of cumulus towers. It is difficult to validate the partitioning between CW and CI since global observations of the ice water path are not readily available. Lin and Rossow (1994) showed that the ice water path may be estimated from the differences between the ISCCP total water path and the SSM/I liquid water path for cold nonprecipitating clouds. Furthermore, their results showed that, in the winter hemisphere, the ice water path of cold nonprecipitating clouds is about three times greater than the liquid water path and only one-half the liquid water path in the summer hemi-

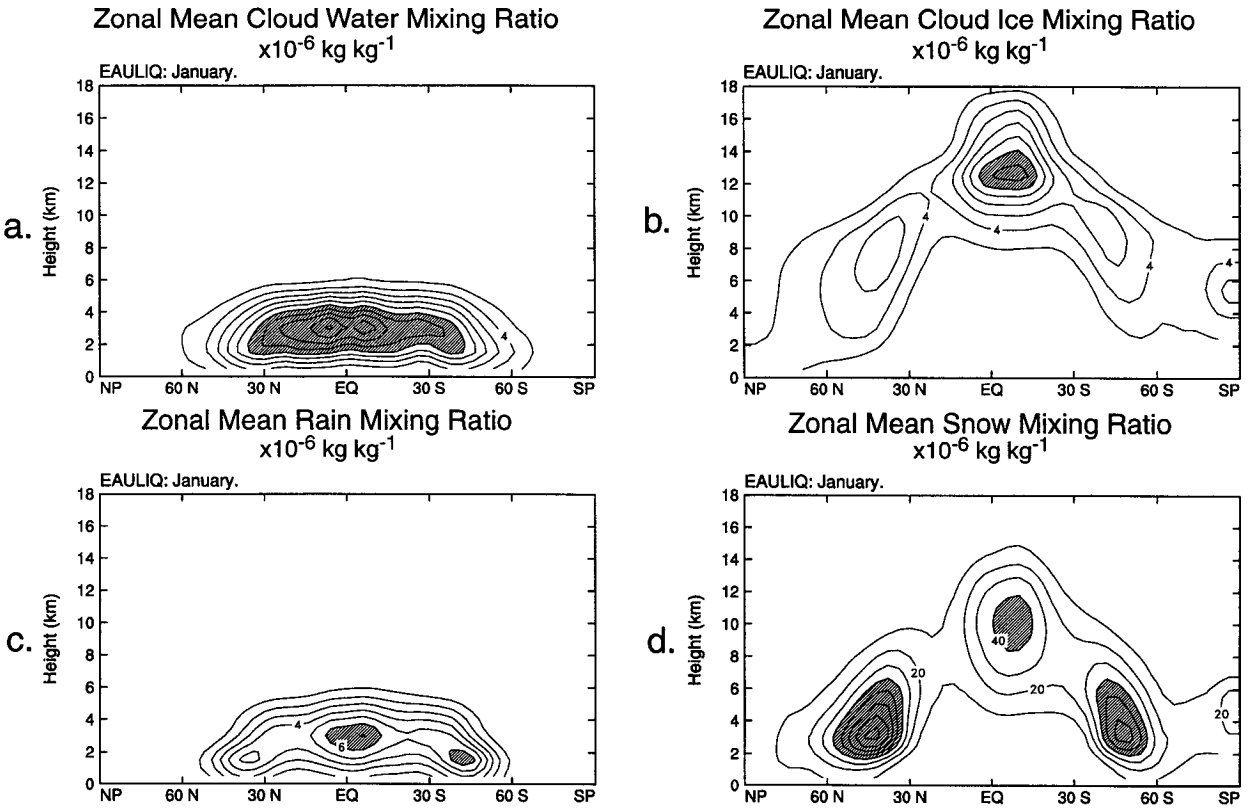

FIG. 7. Latitude–height cross sections of the monthly averaged mixing ratios of (a) cloud water, (b) cloud ice, (c) rain, and (d) snow for January. Units are 10^{-6} kg kg^{-1}. Contour intervals are every 2×10^{-6} kg kg^{-1} for cloud water, 2×10^{-6} kg kg^{-1} for cloud ice, 1×10^{-6} kg kg^{-1} for rain, and 10×10^{-6} kg kg^{-1} for snow, respectively. Shading corresponds to values greater than 12×10^{-6} kg kg^{-1} for cloud water, 12×10^{-6} kg kg^{-1} for cloud ice, 6×10^{-6} kg kg^{-1} for rain, and 40×10^{-6} kg kg^{-1} for snow.

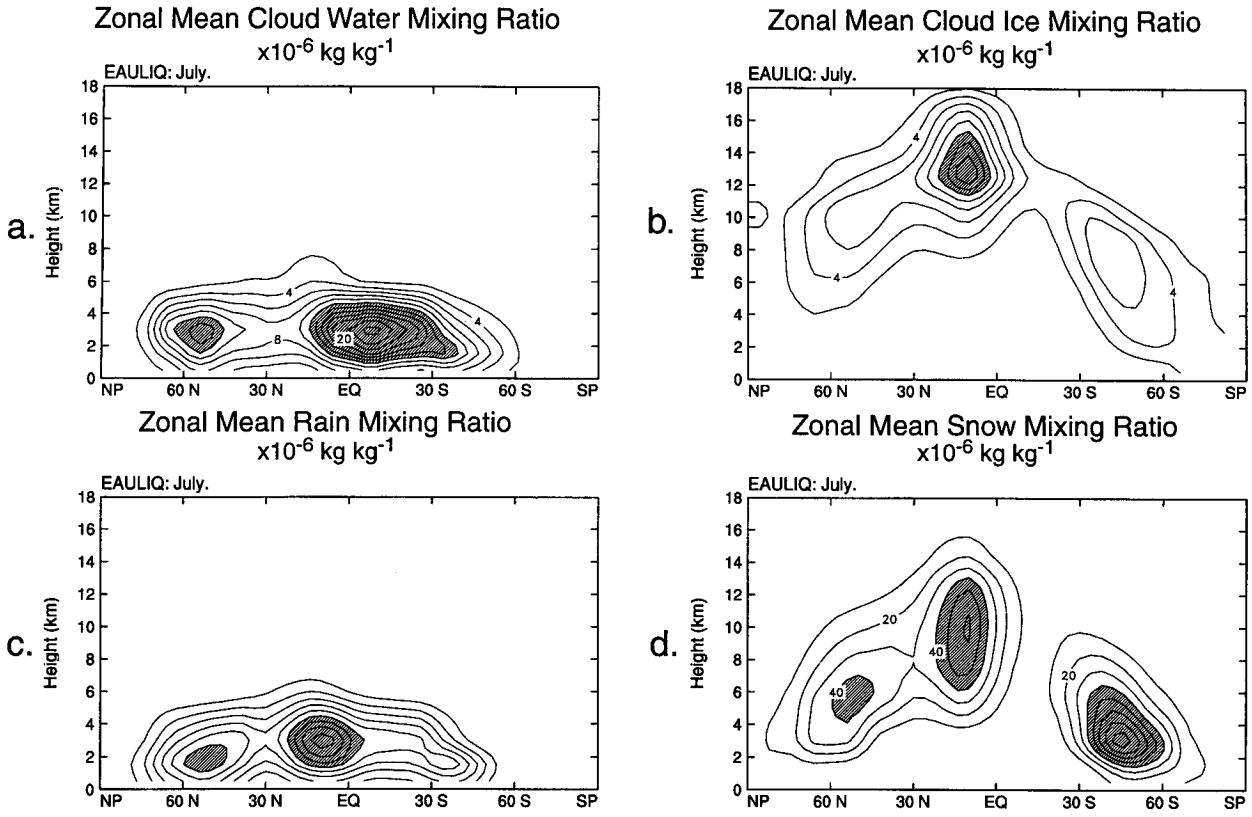

FIG. 8. As Fig. 7 but for July.

sphere. Our results on the partitioning between CW and CI do not agree with the finding of Lin and Rossow (1994). Comparing Fig. 5a against Fig. 5c indicates that maxima in CW actually are twice as large as maxima in CI above the North Pacific and North Atlantic storm track regions. A detailed comparison needs to be undertaken to understand the origins of the discrepancies between the partitioning of the simulated and satellite-derived cloud water and cloud ice paths.

Because rain and snow are produced by autoconversion and collection of cloud water and cloud ice, there is a strong correspondence between the distributions of CW and RW, and CI and RI. In January and July, RW is largest over the tropical convective activity centers and results from autoconversion and collection of cloud water by rain plus melting of snow falling in from aloft. The contribution of melting snow to RW is quite significant and results from the strong removal of cloud ice from the upper troposphere by autoconversion of cloud ice to snow. In contrast, RI is largest at high latitudes and results from autoconversion and collection of cloud ice by snow (enhanced by the Bergeron–Findeisen process) and, much less importantly, from freezing of rain. The latitude–height distribution of RI is similar to that of CI except that the maxima of RI are of course located below those of CI.

c. *Comparison between simulated and satellite-derived CW*

There are major difficulties in trying to compare our results with observations. These difficulties result from our poor knowledge of the global distributions of the various components of the atmospheric hydrologic cycle, except for vertically integrated water vapor. While columnar cloud water estimates retrieved from microwave satellite data are becoming increasingly available for the global oceans (Njoku and Swanson 1983; Prabhakara et al. 1983; Greenwald et al. 1993), similar estimates for the continents are nonexistent. The only data available for the continents are based on local cloud water measurements, and these are difficult to use for global model evaluations because of temporal and spatial scale differences. The amount of cloud ice suspended in the global atmosphere remains completely unknown. One way to evaluate our results is to compare the cloud radiative forcing that the simulated cloud water, cloud ice, and snow produce against the abundant satellite observations from ERBE. Comparisons between the simulated and observed radiation budgets and cloudiness are discussed in Part II.

We compare the simulated CW against columnar cloud water data retrieved from SSM/I observations

over the oceans (Greenwald et al. 1993). Figure 9 shows monthly mean global distributions of the vertically integrated CW retrieved from SSM/I measurements, as well as the zonally averaged profiles of the simulated and satellite-derived CW. January and July maps of the observed CW correspond to ensemble averages obtained between 1988 and 1991.

Although the model qualitatively reproduces the basic geographical features seen in the satellite data, there are quantitative differences between the simulation and the observations. One major discrepancy is that the model underpredicts CW along the ITCZ, as very clearly seen when comparing Figs. 5 and 6 with Fig. 9 and comparing the zonally averaged distributions of the simulated and observed CW, especially in July. In the observations, the ITCZ is very well delineated as a narrow band of high cloud water amounts across the Pacific and Atlantic Oceans. Although the simulated ITCZ is also clearly marked across both oceans, it is not as well delineated as in the observations. The model strongly underestimates CW in the middle latitudes of both hemispheres, especially in July. We suspect that collection of supercooled cloud water by snow may be responsible for the overdepletion of cloud water above the major storm track regions. The impact of this microphysical process upon the magnitude of CW and RW is presently being analyzed. The difference between the simulated and satellite-derived CW also partially results because the cloud microphysics parameterization is not applied in the PBL. We thus expect the simulated CW to be less than that observed. In particular, comparison of the January maps between Figs. 5 and 9 shows that the model strongly underestimates CW over the Southern Ocean.

Before drawing any definitive conclusions on the ability of the cloud microphysics scheme to predict the actual cloud water amount, we need to keep in mind that the retrieval of cloud water from microwave measurements is far from trivial, even over the oceans. Greenwald et al. (1993) caution that satellite-derived cloud water estimates have a theoretical relative error typically ranging between 25% and 40%, depending on the atmospheric and surface conditions and the amount of liquid water present in the cloud. Also, retrievals are known to be less accurate in precipitating than nonprecipitating cloud systems due to contamination by rain drops. SSM/I does not "see" large, precipitating drops; in effect, it senses only drops smaller than some threshold radius. Similarly, the cloud water variable of EAULIQ does not include large, precipitating drops; it represents only the liquid water mass associated with drops smaller than some threshold radius. A problem, however, is that these two threshold radii are not necessarily the same, and we are unable, at this stage, to clearly define the relationship between them. This problem complicates the interpretation of discrepancies between the simulated and SSM/I-observed cloud water distributions.

Global averages of CW, CI, RW, and RI are summarized in Table 4. The bulk cloud microphysics parameterization produces a globally averaged cloud water amount about three times larger than that of cloud ice for both January and July. As already mentioned, there are no available global observations to test this result against. The partitioning between cloud water and cloud ice depends on temperature and the relative rates of detrainment of cloud water and cloud ice at the tops of cumulus towers. Because most of the troposphere is colder than 0°C and the cumulus parameterization detrains more cloud ice than cloud water, the cloud microphysics scheme has a tendency to form an optically thick upper-tropospheric cloud ice shield. The removal of cloud water and cloud ice is strongly controlled by the prescribed thresholds for autoconversion. Although important, collection processes have less influence on the simulated cloud water and cloud ice amounts. As discussed in section 2d, we tuned the thresholds for autoconversion of cloud water to rain (q_{c0} is set equal to 0.25 g kg^{-1}) and cloud ice to snow (q_{i0} is set equal to 0.01 g kg^{-1}) so that 1) the simulated grid averaged cloud water is in reasonable agreement with satellite-derived cloud water estimates and 2) the globally averaged top of the atmosphere outgoing infrared radiation and planetary albedo agree fairly well with ERBE, as discussed in Part II. The rapid autoconversion of cloud ice to snow makes snow the second most abundant water species after water vapor. This is also favored by the slow fall speed of snow (on the order of 2 m s^{-1}).

We repeat here our earlier comment that our results are strongly influenced by the fact that fractional cloudiness is not parameterized; that is, we do not distinguish between local and gridbox mean amounts of cloud water and cloud ice. If we allowed the possibility that model grid points were partially cloudy instead of overcast, the local cloud water occupying the cloudy part of the box would be larger than its equivalent gridbox mean. Autoconversion rates would then increase and prescribed thresholds for autoconversion would have to be increased to obtain the same results presented here. See Fowler and Randall (1994) for further discussion.

5. The moisture budgets of EAULIQ and CONTROL

We now focus on the differences in the hydrologic cycles simulated by EAULIQ and CONTROL.

One major difference between EAULIQ and CONTROL is in the treatment of the water detrained from the tops of cumulus towers. As we discussed earlier, in CONTROL, the cumulus parameterization immediately evaporates the amount of detrained water, and the temperature is corrected accordingly. The large-scale saturation routine then recondenses the vapor, but it produces only liquid, not ice. In EAULIQ, the de-

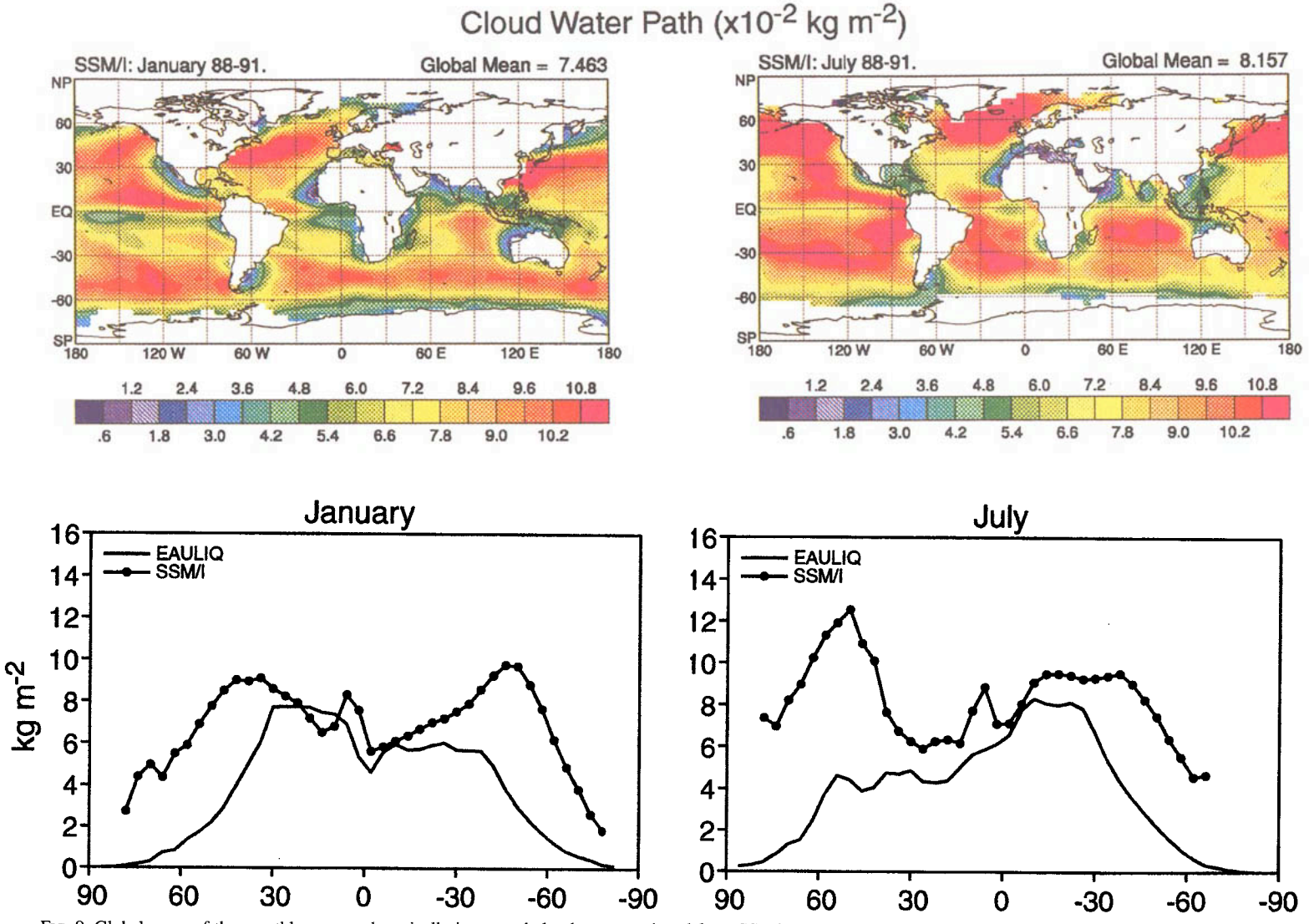

FIG. 9. Global maps of the monthly averaged vertically integrated cloud water retrieved from SSM/I satellite data and zonally averaged distributions of the monthly averaged vertically integrated cloud water simulated by EAULIQ for January and July. Units are 10^{-2} kg m^{-2} for the maps and kg m^{-2} for the zonal profiles, respectively.

TABLE 4. Globally averaged values of the different components of the hydrologic cycle simulated with EAULIQ and CONTROL for January and July.

Hydrologic cycle components	January		July	
	EAULIQ	CONTROL	EAULIQ	CONTROL
Water vapor (kg m^{-2})	22.79	22.87	25.18	24.63
Cloud water (kg m^{-2})	0.043		0.046	
Cloud ice (kg m^{-2})	0.019		0.018	
Rain (kg m^{-2})	0.016		0.0019	
Snow (kg m^{-2})	0.137		0.140	
Cumulus precipitation rate (mm day^{-1})	1.62	2.22	1.75	2.45
Large-scale precipitation of rain (mm day^{-1})	1.33		1.44	
Large-scale precipitation of snow (mm day^{-1})	0.66		0.53	
Total large-scale precipitation (mm day^{-1})	1.99	1.64	1.97	1.41
Total precipitation (mm day^{-1})	3.61	3.86	3.72	3.86

trained cloud water and cloud ice are used as sources of cloud water and cloud ice for the cloud microphysics.

This difference between EAULIQ and CONTROL has a strong impact on the vertical distribution and intensity of the cumulus water vapor moistening rates, as shown in Fig. 10, for January. Negative (positive) production rates correspond to drying (moistening). In CONTROL, cumulus convection dries the atmosphere from the top of the PBL to the tropopause and strongly moistens the upper troposphere. Drying is strongest at about 3 km and rapidly decreases upward, but also shows a secondary maximum at about 8 km. In EAULIQ, little moistening of the upper-troposphere occurs since the detrained cloud water and cloud ice are provided to the cloud microphysics parameterization without any phase change, and the water vapor mixing ratio in the detrained air is necessarily small because of the cold temperatures. Also, EAULIQ yields a significant decrease in the cumulus drying of the middle troposphere, apparently due to a decrease in cumulus activity.

Figure 11 shows latitude–height cross sections of the zonally averaged water vapor mixing ratio (WV) simulated with EAULIQ and CONTROL, and its difference between EAULIQ and CONTROL, for January and July. EAULIQ produces a moistening of the low subtropical troposphere in the summer hemisphere that extends to the middle troposphere in the Tropics. EAULIQ yields a drying of the lower and upper tropical troposphere, as well as a drying of the atmosphere below 4 km poleward of 40°N and 30°S in both January and July. The enhanced moistening of the Tropics is consistent with the decreased drying shown in Fig. 10. The increase in WV in the summer hemisphere is larger in July than in January. As shown in Fig. 12, there is little change in the zonally averaged distribution of WV between EAULIQ and CONTROL. Comparisons between the vertically integrated WV simulated with EAULIQ and CONTROL against that retrieved from SSM/I data for the oceans indicate that EAULIQ and CONTROL have a tendency to underestimate WV in the Tropics and overestimate WV in middle latitudes of the winter hemisphere in both months. Figure 12 also shows that both EAULIQ and CONTROL underestimate WV in the Northern Hemisphere in July.

Latitude–height cross sections of the zonally averaged large-scale relative humidity obtained with EAULIQ and CONTROL are shown in Fig. 13. As discussed earlier, there is a major difference in the computation of relative humidity between the two runs. In EAULIQ, relative humidity is obtained by computing the saturation vapor pressure with respect to ice when the temperature is less than 0°C and by linear interpolation between the saturation vapor pressures with respect to ice and water in the temperature range $-20°C < T \leq 0°C$. In CONTROL, the relative humidity at temperatures less than 0°C is computed using the saturation vapor pressure with respect to water since the ice phase is not included in CONTROL's large-scale saturation parameterization. Because the saturation vapor pressure with respect to ice is smaller than that with respect to liquid water, we expect EAULIQ to produce large relative humidities more easily than CONTROL, at temperatures less than freezing.

At low latitudes, for both January and July, the relative humidity simulated with EAULIQ is increased in the middle troposphere relative to CONTROL and decreased both above and below its local maximum at about 14 km. In middle and high latitudes, the upper-tropospheric relative humidity simulated by EAULIQ is strongly increased in the winter hemisphere, so that a narrow band of high relative humidity extends from pole to pole following the tropopause. The relative humidity is also strongly reduced above the tropopause. Interestingly, the peak in the relative humidity located at 60° of latitude in the winter hemisphere at the 8-km level coincides with a secondary maximum in the amount of cloud ice, as shown previously in Fig. 8. The decrease in the tropical upper-tropospheric relative humidity simulated with EAULIQ is also consistent with the weakening of cumulus activity, as discussed above.

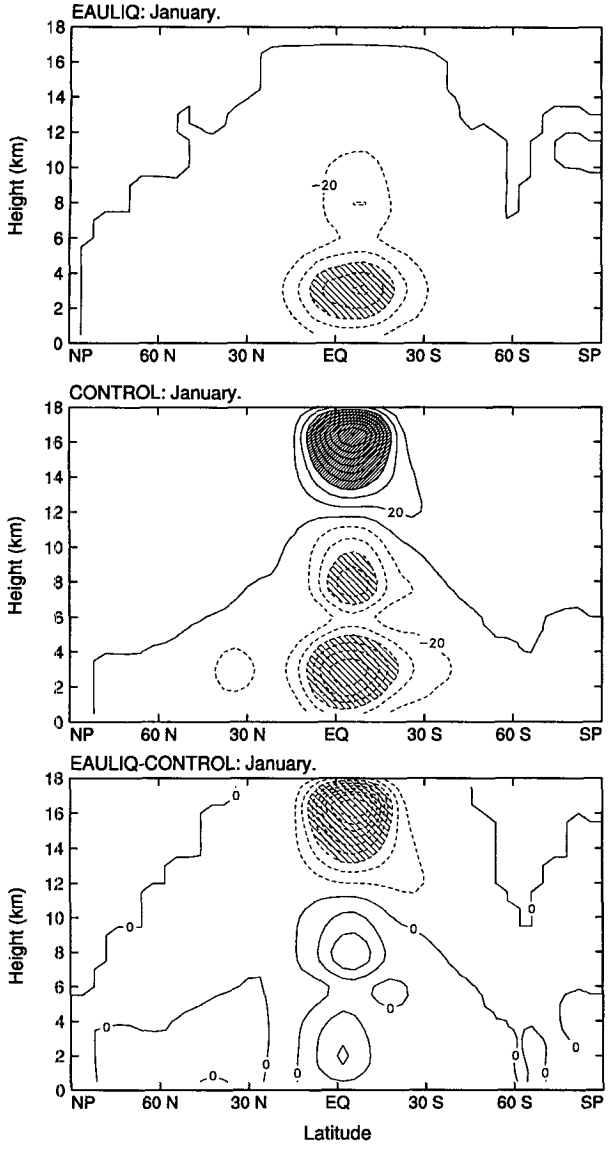

FIG. 10. Latitude–height cross sections of the monthly averaged cumulus water vapor moistening rates simulated with EAULIQ and CONTROL and its difference EAULIQ minus CONTROL for January. Units are 10^{-5} kg kg^{-1} day^{-1} and contour intervals are every 20×10^{-5} kg kg^{-1} day^{-1}. Light shading corresponds to values less than -60×10^{-5} kg kg^{-1} day^{-1}, and heavy shading corresponds to values greater than 60×10^{-5} kg kg^{-1} day^{-1}.

The difference in relative humidity between the two runs may be explained as follows. In CONTROL, detrained condensate is immediately evaporated, as explained earlier, leading to a cooling of the tropical upper troposphere, enhancing its water vapor content and tending to produce supersaturation. In EAULIQ, the frequency of occurrence of supersaturation due to convective detrainment is reduced because the detrained water acts as a source of cloud water and cloud ice (in the Tropics, essentially cloud ice). Cloud water and cloud ice may evaporate, but at a slower rate than in CONTROL, or they can be converted to rain or snow and fall out.

Global maps of the total precipitation rates (TP) obtained with EAULIQ and CONTROL are plotted in Figs. 14 and 15 for January and July. Also, Figs. 14 and 15 display global estimates of TP compiled by Legates and Willmott (1990). The partitioning of TP between cumulus (CP) and large-scale (LP) precipitation rates are shown in Figs. 16 and 17 for January and July. Figure 18 displays zonally averaged profiles of the various precipitation rates, and their global averages are listed in Table 4.

In EAULIQ, LP is the sum of stratiform rain and stratiform snow. The partitioning between rain and snow depends on the temperature of the layer immediately above the PBL since, at present, the cloud microphysics scheme is not applied to the PBL itself. Rain and snow that form in or fall into the bottom layer of the free troposphere are directly transferred to the model surface. Although snow may form by autoconversion plus collection of cloud ice in the tropical upper-troposphere, it often melts, becoming rain, before it reaches the earth's surface. The only regions where snow actually reaches the surface are the high-latitude storm tracks in the winter hemisphere. The characteristic regions of warm stratiform precipitation are the Tropics, where it supplements cumulus precipitation, and the storm track regions in middle latitudes. Separate maps of the precipitation rates of rain and snow are omitted here for brevity.

Figures 14 and 15 indicate that, at low latitudes, regions of heavy rainfall are also regions of intense convective activity: along the ITCZ, especially over the Pacific Ocean, over the continents (Central and South America, Equatorial and Southern Africa), and for the whole monsoon region across the Indian and western Pacific Oceans. Precipitation is enhanced in the midlatitude storm track regions over the Pacific and Atlantic oceans in January.

The inclusion of cloud microphysics, with explicit time stepping of the precipitation of rain and snow, yields significant differences in the regional distribution and magnitude of TP between EAULIQ and CONTROL, especially in the Tropics. The most striking difference is the decrease in TP over the western Pacific and Indian Oceans between CONTROL and EAULIQ. Comparing Fig. 16 against Figs. 14 and 15, we see that the decrease in TP results almost entirely from reduced *cumulus precipitation* over the whole monsoon area in January and July. Regionally, CP decreases by at least 5 mm day^{-1}, especially in January. Here CP does not exceed 10 mm day^{-1}, except for two small areas in July; LP increases slightly in both months. Although not as dramatic, the decrease in CP between CONTROL and EAULIQ is also seen above South America and southern Africa in January and Central America and Equatorial Africa in July. Over deep tropical con-

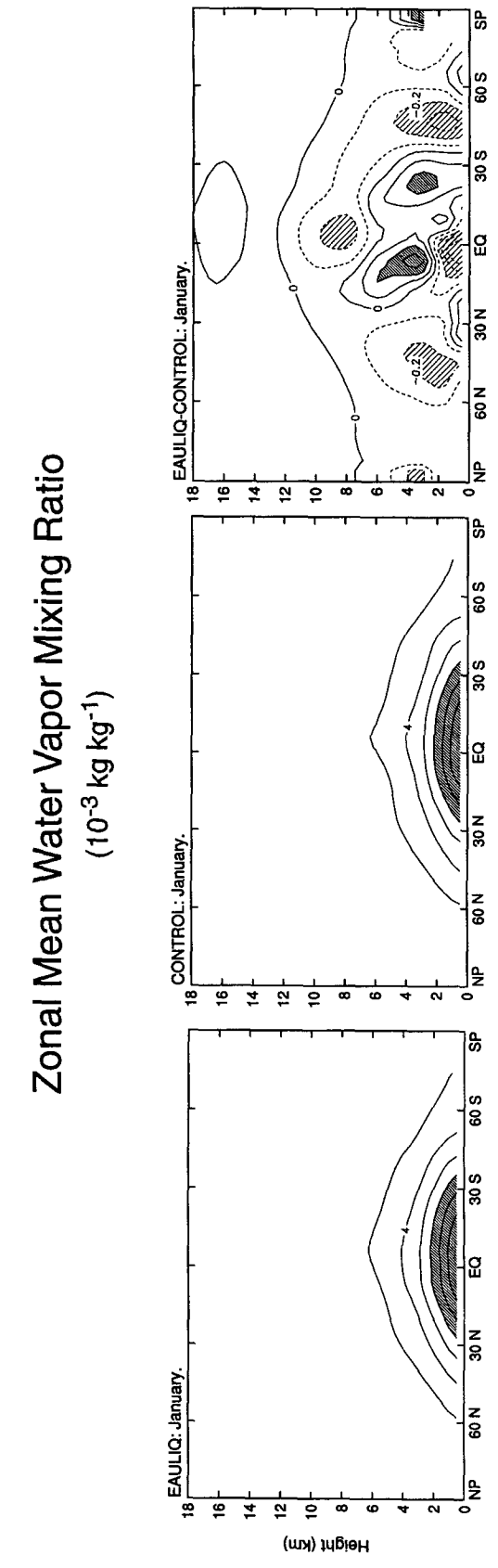

FIG. 11. Latitude–height cross sections of the monthly averaged water vapor mixing ratio simulated with EAULIQ and CONTROL and its difference EAULIQ minus CONTROL for January and July. Units are 10^{-3} kg kg^{-1}. Contour intervals are every 2×10^{-3} kg kg^{-1} (every 0.1×10^{-3} kg kg^{-1} for the difference field). Heavy shading corresponds to values greater than 8×10^{-3} kg kg^{-1}. For the difference field, light shading corresponds to values less than -0.2×10^{-3} kg kg^{-1}, and heavy shading corresponds to values greater than 0.2×10^{-3} kg kg^{-1}.

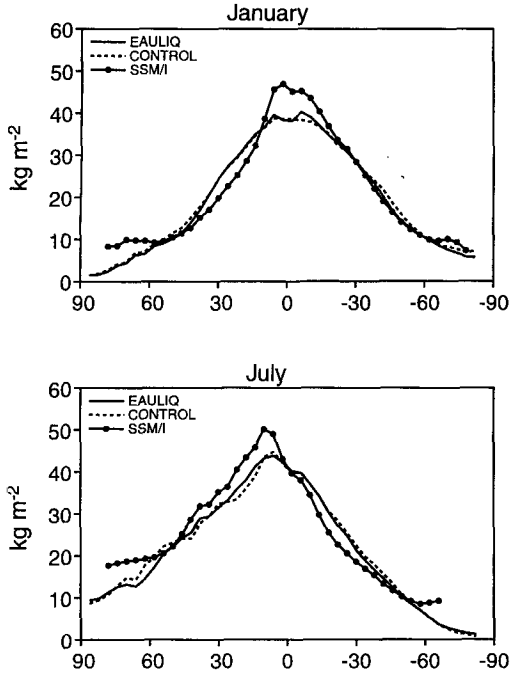

FIG. 12. Zonally averaged distributions of the monthly averaged vertically integrated water vapor simulated with EAULIQ and CONTROL and retrieved from the SSM/I data for January and July. Units are kilograms per square meter.

vective activity centers, the reduced cumulus precipitation rate obtained in EAULIQ is in accordance with the decreased cumulus drying rates seen in Fig. 10.

The decreased CP in EAULIQ, relative to CONTROL, makes TP agree better with the Legates and Willmott climatology over the monsoon area in January and July. However, EAULIQ seems to slightly underestimate TP over the other typical convective activity centers. The zonally averaged distribution is improved when compared against observations, as can be seen in Fig. 18. On a global scale, the decrease in CP in EAULIQ relative to CONTROL (-0.59 mm day^{-1} in January and -0.70 mm day^{-1} in July) is almost compensated by the increase in LP ($+0.35$ mm day^{-1} in January and $+0.55$ mm day^{-1} in July) so that TP varies little between the two simulations. In January, the globally averaged TP is equal to 3.61 mm day^{-1} in EAULIQ versus 3.85 mm day^{-1} in CONTROL. In July, TP is equal to 3.72 mm day^{-1} and 3.87 mm day^{-1} in EAULIQ and CONTROL, respectively.

6. Summary and conclusions

We have described the implementation of a bulk cloud microphysics parameterization that has been designed to simulate stratiform cloudiness. Our objectives were to introduce a physically based representation of the sources and sinks of the main components of the atmospheric moisture budget and to couple the hydrological cycle and radiation through interactive cloud optical properties. The temporal and spatial evolutions of water vapor, cloud water, cloud ice, rain, and snow are determined by various cloud microphysics processes and advective processes. The microphysics of water clouds, mixed-phase clouds, and ice clouds are treated separately. Details of the cloud microphysics parameterization include a continuous collection equation to simulate collection of cloud water and cloud ice by rain and snow, as well as the Bergeron–Findeisen mechanism. An additional feature of the cloud model is the coupling between stratiform clouds and convection through the detrainment of cloud water and cloud ice.

Results of an annual-cycle simulation were discussed for the months of January and July. The cloud microphysics parameterization produces realistic geographical distributions of the vertically integrated cloud water, cloud ice, rain, and snow. Sources of simulated cloud water and cloud ice are located where they should be expected, that is, in the tropical convective activity centers over land and oceans and in the midlatitude storm tracks. In the model, the chief source of cloud water is low-level large-scale supersaturation, whereas detrainment at the tops of cumulus towers is most important for cloud ice, especially in the Tropics. Also, the vertical distribution of cloud ice highlights the importance of deep convection for upper-tropospheric stratiform clouds.

In including a bulk cloud microphysics parameterization developed for mesoscale models into a GCM, one is forced to 1) limit the number of water species and the number of cloud microphysical processes that are included and 2) deal with the tuning of a large possible number of cloud microphysics parameters. For instance, in EAULIQ and in contrast to standard cloud microphysics parameterizations for mesoscale models, hail and graupel were neglected and melting and freezing processes were assumed to be instantaneous. Our cloud microphysics parameterization does not include a prognostic equation for the number concentration of cloud water droplets and cloud ice crystals at this time. The details of ice nucleation were omitted, and we chose, instead, to represent condensation/evaporation and deposition/sublimation processes in a simplified manner by using identical relaxation times.

In terms of adapting the cloud microphysics parameters to the spatial and temporal resolutions of the CSU GCM, we encountered two difficulties.

First, we had to solve the problem of overdepletion of rain and snow due to precipitation by using a 2-minute time step for the microphysical processes, which is quite small compared to time steps currently used in GCMs but also quite large compared to time steps typically used in mesoscale models (for instance, 10 s in Rutledge and Hobbs 1983). If it were not for the problem of explicitly computing the falling rates of rain and snow, we could use a time step as large as the

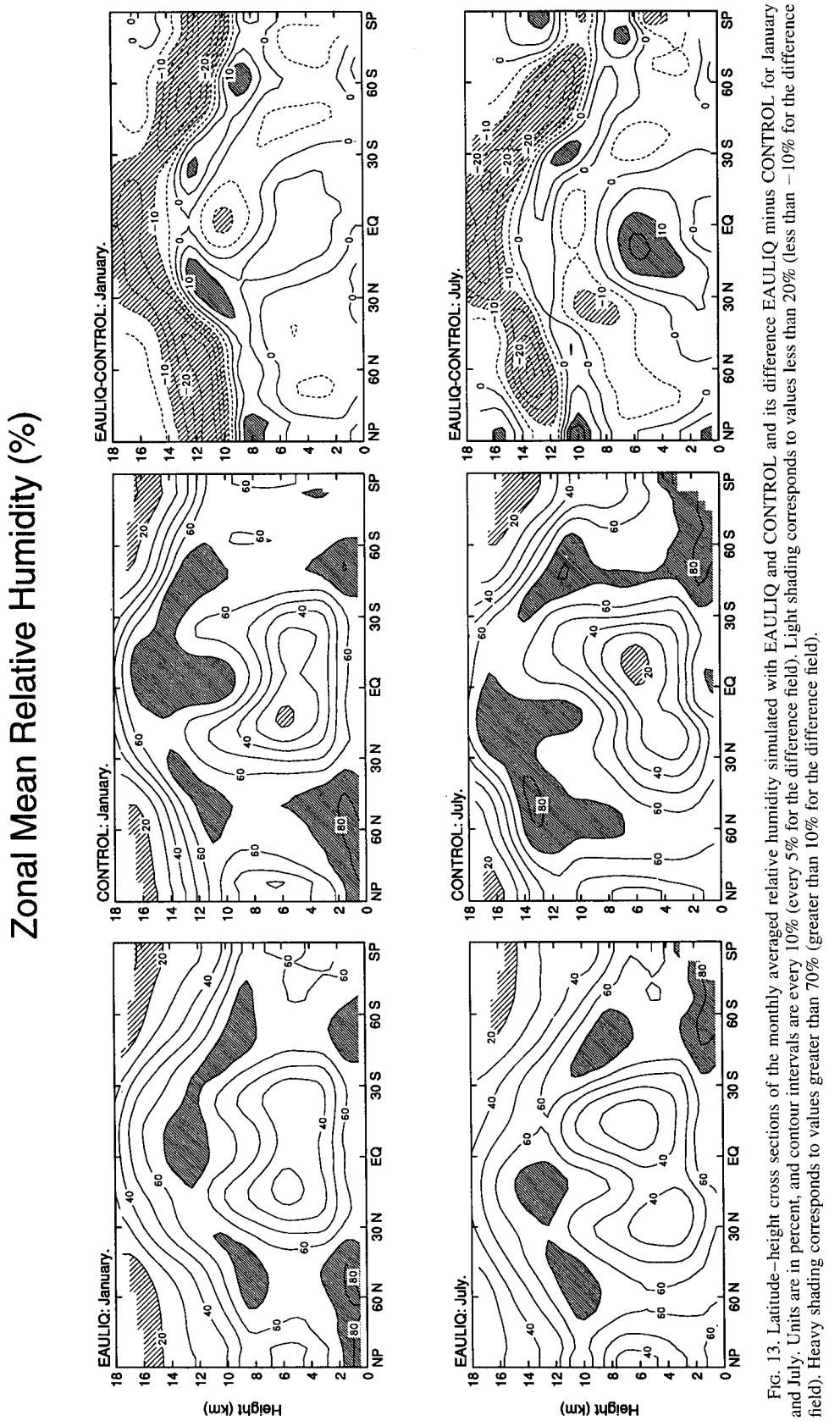

FIG. 13. Latitude–height cross sections of the monthly averaged relative humidity simulated with EAULIQ and CONTROL and its difference EAULIQ minus CONTROL for January and July. Units are in percent, and contour intervals are every 10% (every 5% for the difference field). Light shading corresponds to values less than 20% (less than −10% for the difference field). Heavy shading corresponds to values greater than 70% (greater than 10% for the difference field).

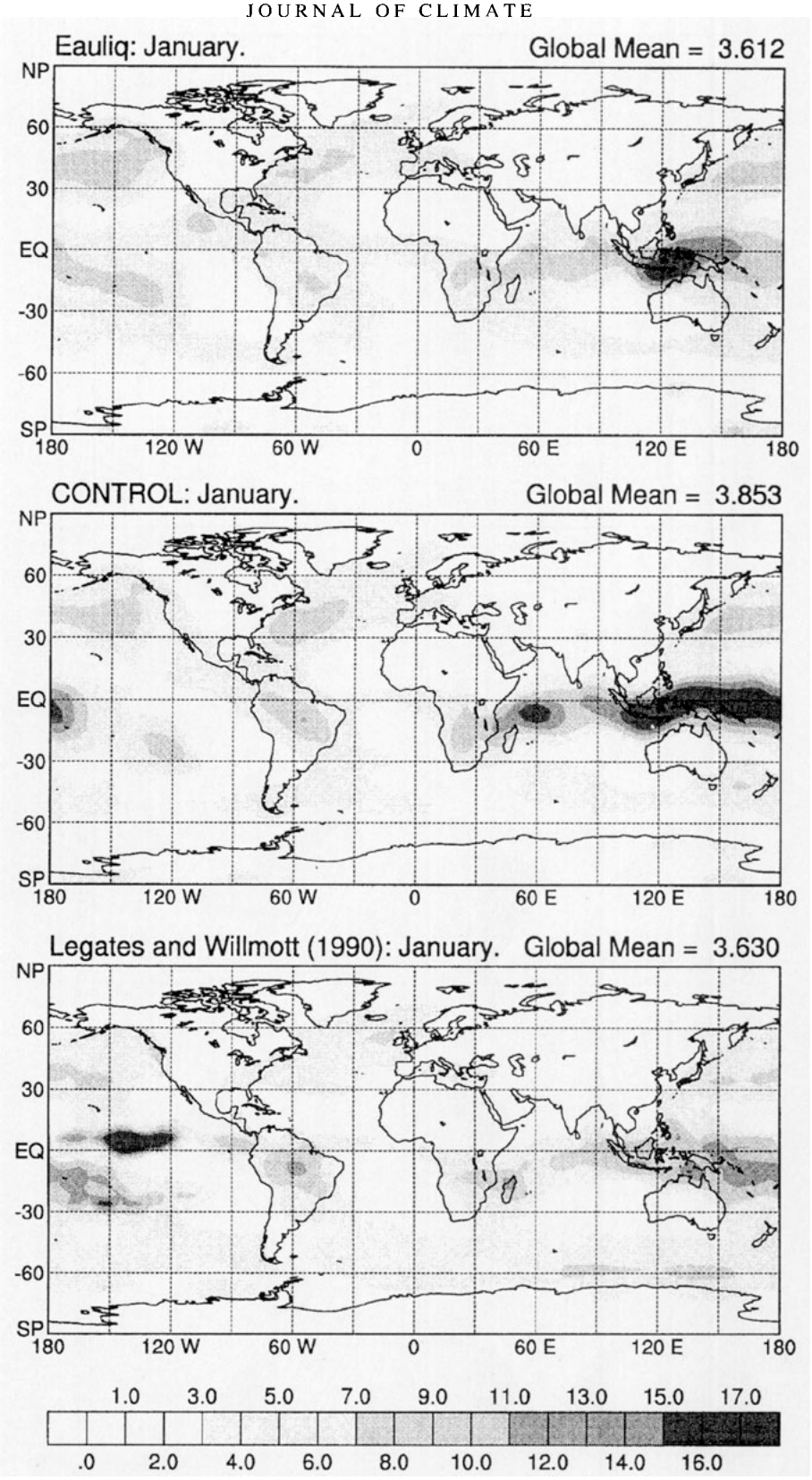

FIG. 14. Global maps of the monthly averaged total precipitation rate simulated with EAULIQ and CONTROL and compiled by Legates and Willmott (1990) for January. Units are millimeters per day.

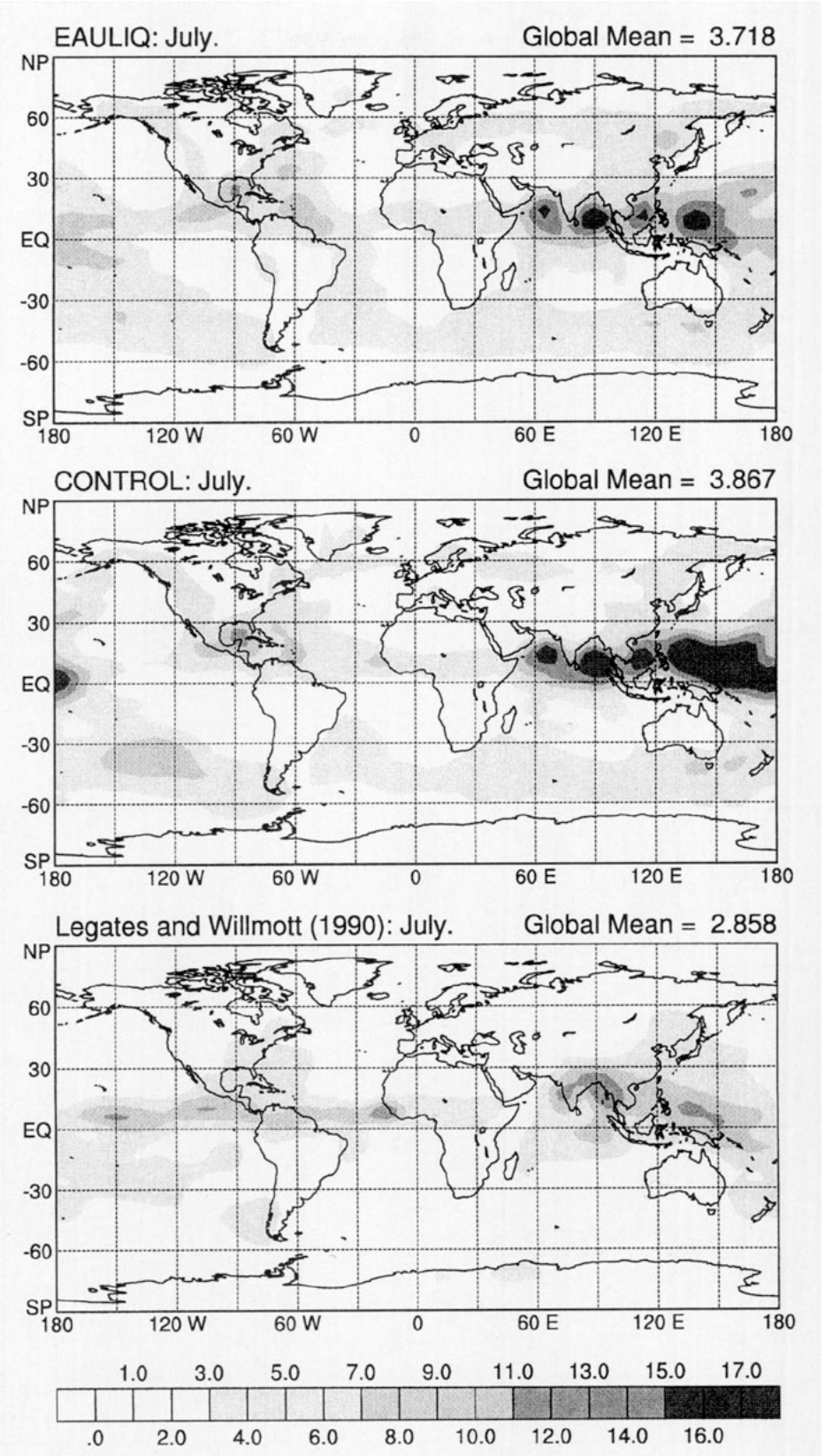

FIG. 15. As Fig. 14 but for July.

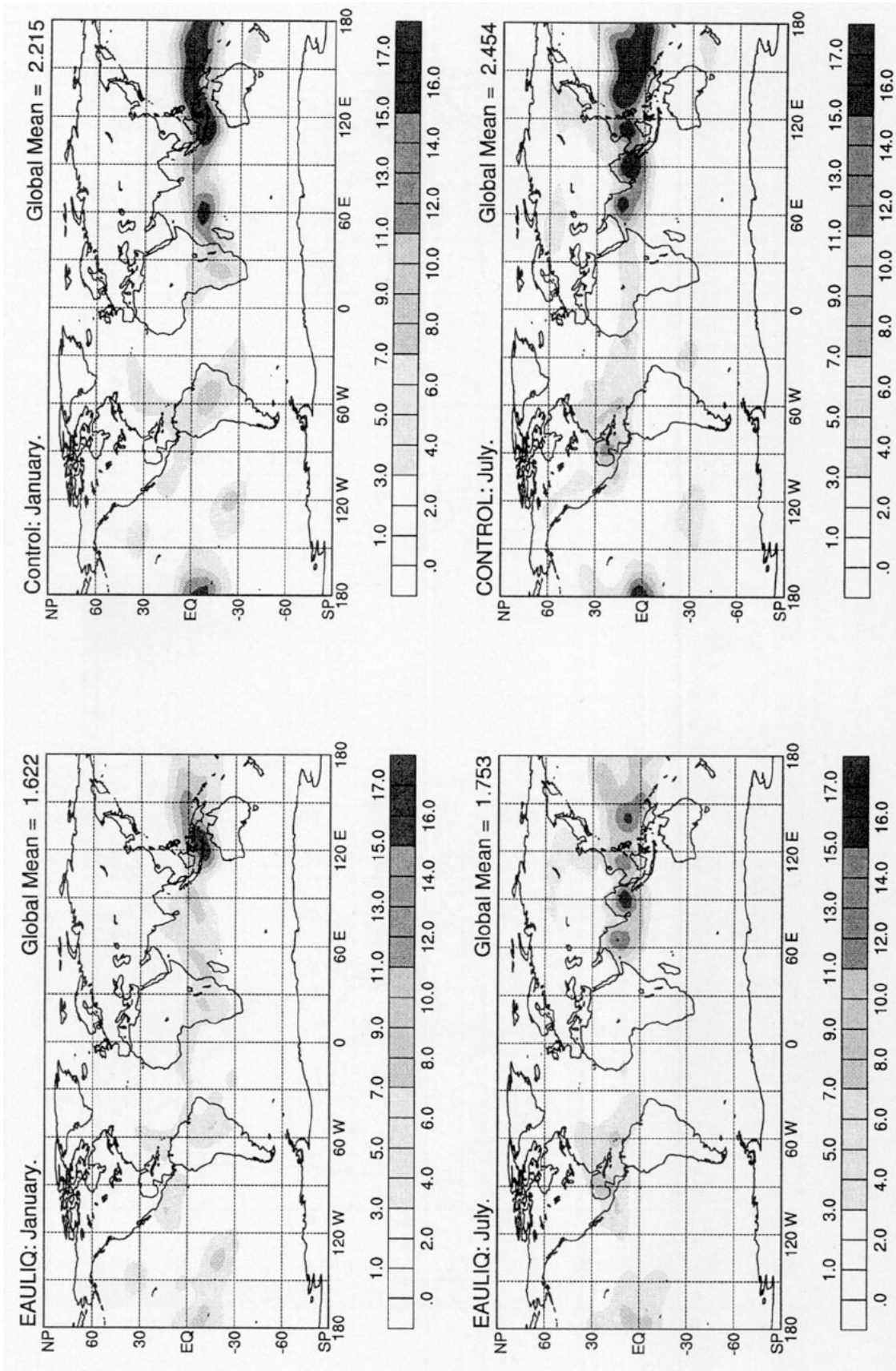

FIG. 16. Global maps of the monthly averaged cumulus precipitation rate simulated by EAULIQ and CONTROL for January and July. Units are millimeters per day.

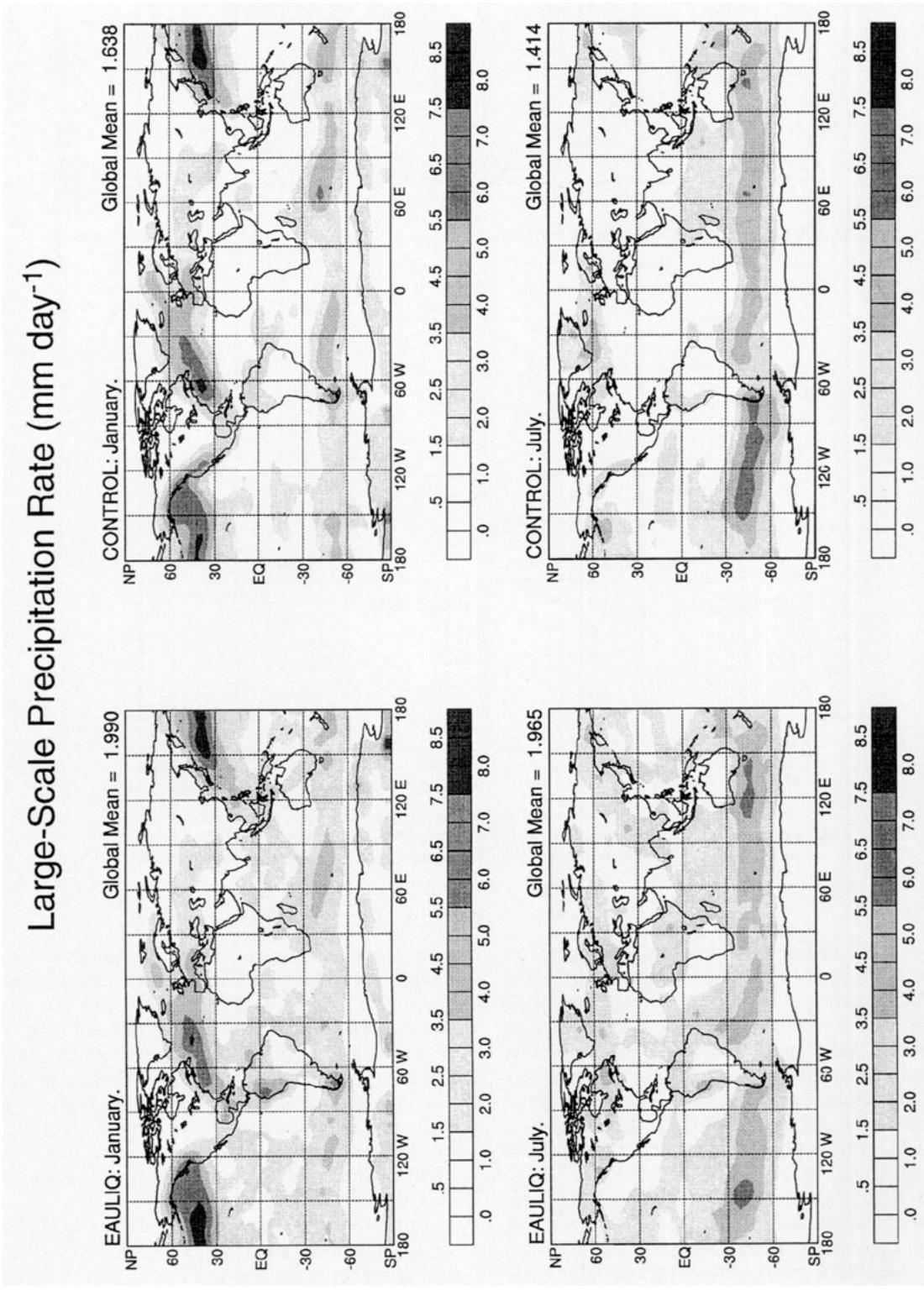

FIG. 17. Global maps of the monthly averaged large-scale precipitation rate simulated with EAULIQ and CONTROL for January and July. Units are millimeters per day.

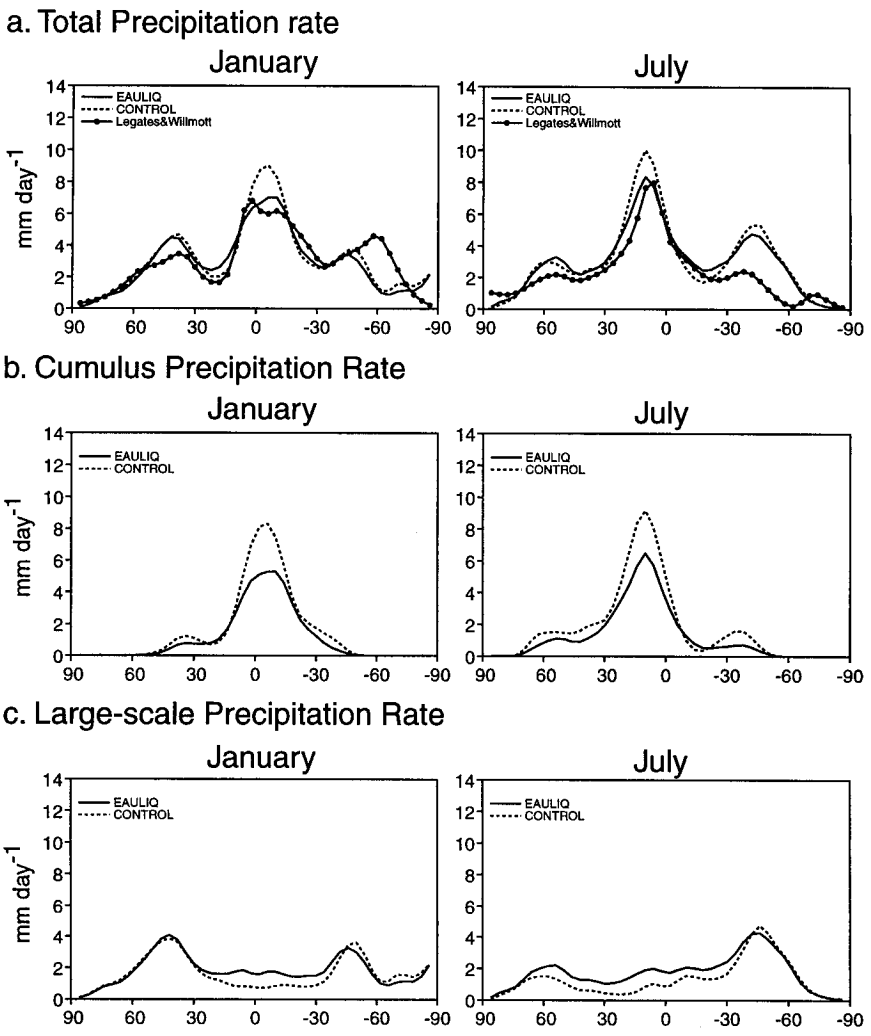

FIG. 18. Zonally averaged distributions of the monthly averaged (a) total, (b) cumulus, and (c) large-scale precipitation rates simulated with EAULIQ and CONTROL and total precipitation rates compiled by Legates and Willmott (1990) for January and July. Units are millimeters per day.

dynamical time step since the time rates of change of the various water species are otherwise computed using a fully implicit scheme. We do not expect that using larger time steps to compute the time rates of change of the different water species would significantly alter their global distributions; this remains to be tested, however. At present, EAULIQ is twice as expensive to run as CONTROL. On a CRAY C-90, EAULIQ uses 220.2 s of CPU time per simulated day versus 110.5 s per day for CONTROL.

Second, we had to decrease the thresholds of autoconversion of cloud water to rain and cloud ice to snow because our current parameterization does not allow for fractional cloudiness, and gridbox-averaged cloud water and cloud ice amounts can be much less than their equivalent local values would be in a partially cloudy gridbox. Here q_{c0} and q_{i0} are the only two parameters that we modified from the original parameterizations of Rutledge and Hobbs (1983, 1984) and Lin et al. (1983). We choose to change these two parameters because their magnitude is clearly linked to the problem of parameterizing fractional cloudiness, and the changes in q_c and q_i due to autoconversion processes are greater than those due to collection. We plan soon to include a parameterization of subgrid-scale cloudiness (Xu and Randall 1994) and foresee that q_{c0} and q_{i0} will then have to be increased to values closer to those used in mesoscale models.

In proposing a new scheme to prognostically determine the temporal and spatial distributions of cloud water, cloud ice, rain, and snow in GCMs, it is important to determine the sensitivity of the simulated climate to the various assumptions made in the cloud microphysics parameterizations.

The most difficult task in evaluating our cloud microphysics scheme is the comparison of our results with observations. Only the global distributions of columnar water vapor and cloud water over the oceans can be compared against estimates from satellites. Although such global observations are extremely valuable, uncertainties inherent to the numerous difficulties in retrieving cloud water data from passive microwave radiation measurements make them far from completely reliable. In addition, global observations of cloud ice are sorely needed.

The impacts of cloud microphysics and interactive cloud optical properties on the simulated radiation budget and cloudiness are analyzed in Part II.

Acknowledgments. This research was sponsored by the National Science Foundation under Grant ATM-8907414, by NASA under Grant NAG-1-1266, and by the ARM program of the U.S. Department of Energy under Grant DE-FG02-92ER61363, all to Colorado State University, and by subcontract 0965G4A007 from the University of Los Angeles, California, under the NASA Grant NAG 5-2224 to UCLA. Computing resources were provided by the Scientific Computing Division at the National Center for Atmospheric Research, by the National Center for Computational Sciences at NASA/Goddard, and by the National Energy Research Supercomputer Center at Lawrence Livermore National Laboratory. We would like to thank D. Dazlich, also of the Department of Atmospheric Science at Colorado State University, for his invaluable assistance in working with the CSU GCM in the early stages of this research. We also thank T. Greenwald and I. Wittmeyer for providing the SSM/I water vapor and cloud water data.

APPENDIX A

Cloud Microphysics Equations

In this appendix, we describe the cloud microphysics equations used in the model. They remain essentially the same as those discussed by Smith and Randall (1992), except for the parameterizations of condensation and deposition and melting of snow. Definitions of variables and constants used below are listed in appendix B.

a. Rain and snow size distributions

The rain and snow particle sizes are assumed to be distributed continuously according to an inverse exponential distribution. Rain is assumed to follow the size distribution derived by Marshall and Palmer (1948), while the size distribution of snow is given by Gunn and Marshall (1958). The assumed size distribution functions for rain and snow may be respectively written as

$$N_{DR} = N_{0R} \exp(-\lambda_R D_R) dD_R \tag{A1}$$

and

$$N_{DS} = N_{0S} \exp(-\lambda_S D_S) dD_S. \tag{A2}$$

The values of N_{0R} and N_{0S} given by Houze et al. (1979) are used. In (A1) and (A2), λ_R and λ_S are the slope factors of the size distributions for rain and snow, respectively. They may be expressed by

$$\lambda_R = \left(\frac{\pi \rho_L N_{0R}}{\rho q_r}\right)^{1/4} \tag{A3}$$

and

$$\lambda_S = \left(\frac{\pi \rho_S N_{0S}}{\rho q_s}\right)^{1/4}. \tag{A4}$$

b. Mass-weighted fall speeds

Rain and snow are assumed to fall at their mass-weighted fall speeds following Rutledge and Hobbs (1983). For rain, this fall speed is given by

$$\bar{V}_R = \frac{\int_0^\infty N_{DR}(D_R) M(D_R) V_R(D_R) dD_R}{\int_0^\infty N_{DR}(D_R) M(D_R) dD_R}, \tag{A5}$$

where $M(D_R) = \pi/6(\rho_L D_R^3)$. Following the experimental results of Gunn and Kinzer (1949), $V_R(D_R)$ may be parameterized as a function of D_R:

$$V_R(D_R) = (-0.267 + 5.15 \times 10^3 D_R - 1.0225 \times 10^6 D_R^2 + 7.55 \times 10^7 D_R^3)\left(\frac{p_0}{p}\right)^{0.4}, \tag{A6}$$

where the drop parameter D_R is in meters and $V_R(D_R)$ is in meters per second. Using (A1), (A5), and (A6), $\bar{V}_R$ may be rewritten as

$$\bar{V}_R = (-0.267 + 206 \times 10^2 \lambda_R^{-1} - 2.045 \times 10^7 \lambda_R^{-2} + 9.06 \times 10^9 \lambda_R^{-3})\left(\frac{p_0}{p}\right)^{0.4}, \tag{A7}$$

where λ_R (in m^{-1}) is given by (A3). The factor $(p_0/p)^{0.4}$ allows for the change in fall speed with air pressure (Foote and Dutoit 1969).

The fall speed for snow is assumed to be

$$\bar{V}_S = \frac{\int_0^\infty N_{DS}(D_S) M(D_S) V_S(D_S) dD_S}{\int_0^\infty N_{DS}(D_S) M(D_S) dD_S}. \tag{A8}$$

Snow is assumed to consist of aggregates of dendrites whose mass-weighted fall speed may be expressed following the expression of Locatelli and Hobbs (1974); that is,

$$V_S(D_S) = a'' D_S^b \left(\frac{p_0}{p}\right)^{0.4}, \quad \text{(A9)}$$

where it is assumed that $M(D_S) = \pi/6(\rho_S D_S^3)$. Using (A2), (A8), and (A9), $\bar{V}_S$ may be written as

$$\bar{V}_S = a'' \frac{\Gamma(4+b)}{6} \lambda_S^{-b} \left(\frac{p_0}{p}\right)^{0.4}, \quad \text{(A10)}$$

where λ_S (in m^{-1}) is given by (A4).

c. Sources and sinks

1) CONDENSATION OF WATER VAPOR/EVAPORATION OF CLOUD WATER (PCOND)

Conversion of water vapor to form cloud water takes place when the water vapor mixing ratio exceeds its saturation value with respect to water and $T \geq T_0$. If $q_v < q_{sw}$ and $q_c > 0$, cloud water evaporates. In contrast to Smith and Randall (1992), where condensation/evaporation was treated as an instantaneous process, we assume that condensation and evaporation occur at finite but rapid rates so that they may be solved implicitly (refer to section 2) following

$$\text{PCOND} = \frac{q_v - q_{sw}}{\tau_w}, \quad \text{if} \quad q_v \geq q_{sw} \quad \text{(A11)}$$

and

$$\text{PCOND} = q_c \left(\frac{S_w - 1}{\tau_w}\right), \quad \text{if} \quad q_v < q_{sw}. \quad \text{(A12)}$$

In (A11) and (A12), τ_w is a prescribed relaxation time, which is set equal to 100 s.

2) AUTOCONVERSION OF CLOUD WATER (PRAUT)

Collisions of cloud water droplets can be a source of rain. Following Kessler (1969), the autoconversion rate of cloud water to rain (PRAUT) may be written as

$$\text{PRAUT} = \alpha(q_c - q_{c0}), \quad \text{if} \quad q_c \geq q_{c0}, \quad \text{(A13)}$$

where α is a rate coefficient and q_{c0} is a cloud water threshold for autoconversion. The value of α given by Kessler (1969) is used. PRAUT is not an instantaneous process. It is highly sensitive to the threshold value q_{c0}, which is set equal to 0.25×10^{-3} kg kg^{-1}, while changes in α do not strongly affect the overall microphysics (Weinstein 1970).

3) COLLECTION OF CLOUD WATER BY RAIN (PRACW)

The collection of cloud water by rain is assumed to follow the continuous collection equation:

$$\frac{d}{dt} M(D_R) = \frac{\pi}{4} E_{RC} D_R^2 V_R(D_R). \quad \text{(A14)}$$

Multiplying (A14) by (A1) and integrating (A14) over all drop sizes yields

$$\text{PRACW} = \frac{\pi}{4} E_{RC} N_{0R} q_c \left(\frac{p_0}{p}\right)^{0.4} \times \left[\frac{a_0\Gamma(3)}{\lambda_R^3} + \frac{a_1\Gamma(4)}{\lambda_R^4} + \frac{a_2\Gamma(5)}{\lambda_R^5} + \frac{a_3\Gamma(6)}{\lambda_R^6}\right]. \quad \text{(A15)}$$

We prefer to express (A15) in terms of q_c and q_r using the condensed form

$$\text{PRACW} = \text{FCR} q_c q_r, \quad \text{(A16)}$$

where

$$\text{FCR} = \frac{E_{RC}}{4} \left(\frac{\rho}{\rho_L}\right) \left(\frac{p_0}{p}\right)^{0.4} \times \left[a_0\Gamma(3)\lambda_R + a_1\Gamma(4) + \frac{a_2\Gamma(5)}{\lambda_R} + \frac{a_3\Gamma(6)}{\lambda_R^2}\right]. \quad \text{(A17)}$$

4) EVAPORATION OF RAINWATER (PREVP)

Evaporation of rain (PREVP) is assumed to occur if the air is subsaturated with respect to water and if the evaporation of cloud water (PCOND) is insufficient to remove the subsaturation. Similarly, if the air is supersaturated with respect to water, growth by condensation may occur. From Byers (1965), the continuous growth equation may be written as

$$\frac{d}{dt} M(D_R) = \frac{2\pi D_R (S_w - 1) F}{A' + B'}, \quad \text{(A18)}$$

where

$$A' = \frac{L_v}{K_a T} \left(\frac{L_v M_w}{R^* T} - 1\right) \quad \text{(A19)}$$

and

$$B' = \frac{R^* T}{\chi M_w e_{sw}}. \quad \text{(A20)}$$

The values of A' and B' given by Pruppacher and Klett (1978) are used. In (A18), F is a "ventilation factor," which may be written as (Beard and Pruppacher 1971)

$$F = 0.78 + 0.31 S_c^{1/3} R_e^{1/2}. \quad \text{(A21)}$$

The total evaporation rate is then obtained by substituting (A21) into (A18), multiplying (A18) by (A1), and integrating over all drop sizes, giving

$$\text{PREVP} = \frac{2\pi N_{0R} (S_w - 1)}{\rho_L (A' + B')} \times \left[\frac{0.78}{\lambda_R^2} + 0.31 \frac{\left(a' \frac{\rho}{\mu}\right)^{1/2}}{\lambda_R^3} \Gamma(3) \left(\frac{P_0}{p}\right)^{0.2}\right]. \quad \text{(A22)}$$

Equation (A22) may also be simply expressed as a function of S_w and q_r:

$$\text{PREVP} = \text{FRV}\,(S_w - 1)\,q_r, \qquad \text{(A23)}$$

where

$$\text{FRV} = \frac{2}{\rho_L(A' + B')} \times \left[0.78\lambda_R^2 + 0.31\left(a'\frac{\rho}{\mu}\right)^{1/2}\lambda_R\Gamma(3)\left(\frac{p_0}{p}\right)^{0.2}\right]. \qquad \text{(A24)}$$

To make the integration more manageable, it is assumed that $V_R(D_R) = a'D_R$, instead of (A6), which still gives good accuracy.

5) Deposition of water vapor/Evaporation of cloud ice (PSUB)

Deposition of water vapor on cloud ice crystals takes place when the water vapor mixing ratio exceeds its saturation value with respect to ice and $T < T_{00}$. If $q_v < q_{si}$, cloud ice evaporates. As for the condensation rate, we assume that deposition and evaporation occur at finite but rapid rates so that they may be solved implicitly, following

$$\text{PSUB} = \frac{q_v - q_{si}}{\tau_i}, \quad \text{if} \quad q_v \geq q_{si}, \qquad \text{(A25)}$$

and

$$\text{PSUB} = q_i\left(\frac{S_i - 1}{\tau_i}\right), \quad \text{if} \quad q_v < q_{si}. \qquad \text{(A26)}$$

In (A25) and (A26), τ_i is a prescribed relaxation time, which is set equal to 100 s.

6) Autoconversion of cloud ice to snow (PSAUT)

The conversion of cloud ice to snow follows the parameterization originally proposed by Kessler (1969) to simulate the collision–coalescence process for ice crystals. The formulation is similar to (A13); that is,

$$\text{PSAUT} = \beta(q_i - q_{i0}), \quad \text{if} \quad q_i \geq q_{i0}, \qquad \text{(A27)}$$

where β is a temperature-dependent rate coefficient and q_{i0} is a threshold for aggregation whose value is set equal to 0.01×10^{-3} kg kg^{-1}. The relationship used for β is

$$\beta = 10^{-3}\exp[0.025(T - T_0)], \qquad \text{(A28)}$$

which is a crude parameterization of the dependence of aggregation efficiency on crystal structure and is in turn temperature dependent (Pruppacher and Klett 1978).

7) Collection of cloud ice by snow (PSACI)

The collection of cloud ice by snow is parameterized in the same manner as the collection of cloud water by rain (PRACW), using the continuous collection equation

$$\frac{d}{dt}M(D_S) = \frac{\pi}{4}E_{SI}D_S^2V_S(D_S)q_i. \qquad \text{(A29)}$$

Multiplying (A29) by (A2), using (A8), and integrating over all particle sizes yields

$$\text{PSACI} = \frac{\pi a'' q_i E_{SI} N_{0S}}{4}\left(\frac{p_0}{p}\right)^{0.4}\frac{\Gamma(b+3)}{\lambda_S^{b+3}}, \qquad \text{(A30)}$$

where λ_S is given by (A4). Equation (A30) may also be expressed as a function of q_i and q_s; that is,

$$\text{PSACI} = \text{FIS}q_iq_s, \qquad \text{(A31)}$$

where

$$\text{FIS} = \frac{E_{SI}}{4}a''\left(\frac{\rho}{\rho_S}\right)\left(\frac{p_0}{p}\right)^{0.4}\frac{\Gamma(b+3)}{\lambda_S^{b-1}}. \qquad \text{(A32)}$$

8) Collection of cloud water by snow (PSACW)

For $T < T_0$, the collection of cloud water by snow (PSACW) leads to growth of snow by riming. For $T \geq T_0$, PSACW represents the rate at which melting snow accretes cloud droplets, which is a source of rain. The parameterization of the collection of cloud water by snow is similar to (A30):

$$\text{PSACW} = \frac{\pi a'' q_c E_{SC} N_{0S}}{4}\left(\frac{p_0}{p}\right)^{0.4}\frac{\Gamma(b+3)}{\lambda_S^{b+3}}, \qquad \text{(A33)}$$

where the continuous collection equation has been used. As (A30), (A33) may also be written as

$$\text{PSACW} = \text{FCS}q_cq_s, \qquad \text{(A34)}$$

where

$$\text{FCS} = \frac{E_{SC}}{4}a''\left(\frac{\rho}{\rho_S}\right)\left(\frac{p_0}{p}\right)^{0.4}\frac{\Gamma(b+3)}{\lambda_S^{b-1}}. \qquad \text{(A35)}$$

9) Depositional growth of snow (PSEVP)

When the air is supersaturated with respect to ice, the rate of growth of snow by deposition of water vapor (PSEVP) is given by

$$\frac{dM}{dt} = \frac{C}{\epsilon_0}\frac{(S_i - 1)}{A'' + B''}, \qquad \text{(A36)}$$

where $C = 4D_S\epsilon_0$ is the capacitance of snow and D_S is the average diameter of the snow particles. In (A36),

$$A'' = \frac{L_s}{K_a T}\left(\frac{L_s M_w}{R^* T} - 1\right) \quad \text{(A37)}$$

and

$$B'' = \frac{R^* T}{\chi M_w e_{si}} \quad \text{(A38)}$$

are given by Pruppacher and Klett (1978). Multiplying (A36) by (A2) and integrating over all particle sizes, we obtain

$$\text{PSEVP} = \frac{4(S_i - 1)N_{0S}}{\rho(A'' + B'')} \times \left[\frac{0.65}{\lambda_S^2} + 0.44\left(\frac{a''\rho}{\mu}\right)^2\left(\frac{p_0}{p}\right)^{0.2}\frac{\Gamma\left(\frac{b}{2}+\frac{5}{2}\right)}{\lambda_S^{b/2+5/2}}\right]. \quad \text{(A39)}$$

We may express PSEVP as

$$\text{PSEVP} = \text{FSV}(S_i - 1)q_s, \quad \text{(A40)}$$

where

$$\text{FSV} = \left(\frac{4}{\pi\rho_S(A'' + B'')}\right) \times \left[0.65\lambda_S^2 + 0.44\left(\frac{a''\rho}{\mu}\right)^2 \times \left(\frac{p_0}{p}\right)^{0.2}\Gamma\left(\frac{b}{2}+\frac{5}{2}\right)\lambda_S^{(3/2-b/2)}\right]. \quad \text{(A41)}$$

10) MELTING OF CLOUD ICE/FREEZING OF CLOUD WATER (PSMLTI) AND MELTING OF SNOW/FREEZING OF RAIN (PSMLTS)

Cloud ice is a source of cloud water upon melting ($T \geq T_0$), and cloud water is a source of cloud ice upon freezing ($T < T_{00}$). Melted snow is a source for rain ($T \geq T_0$). Rain is a source of snow upon freezing ($T < T_{00}$). Both melting/freezing processes are assumed to occur instantaneously and are given by

$$\text{PSMLTI} = \frac{q_i}{\Delta t}(T \geq T_0)$$

$$\text{and} \quad \text{PSMLTI} = -\frac{q_c}{\Delta t}(T < T_{00}) \quad \text{(A42)}$$

and

$$\text{PSMLTS} = \frac{q_s}{\Delta t}(T \geq T_0)$$

$$\text{and} \quad \text{PSMLTS} = -\frac{q_r}{\Delta t}(T < T_0). \quad \text{(A43)}$$

d. The Bergeron–Findeisen process

As discussed in section 2, cloud water and cloud ice are allowed to coexist in the temperature range $T_{00} < T \leq T_0$. If $T_{00} < T \leq T_0$, we express the conversion of water vapor to ice and water, and the conversion of the total condensate $q_c + q_i$ to water vapor (PBERG), by expressions similar to (A11) and (A25), and (A12) and (A26), respectively:

$$\text{PBERG} = \frac{q_v - q_{sm}}{\tau_m} \quad \text{if,} \quad q_v \geq q_{sm}, \quad \text{(A44)}$$

and

$$\text{PBERG} = (q_c + q_i)\left(\frac{S_{sm} - 1}{\tau_m}\right), \quad \text{if} \quad q_v < q_{sm}. \quad \text{(A45)}$$

PSEVP remains as in (A40), except that S_i is replaced by the interpolated saturation S_{sm}. In (A44)–(A45), τ_m is set equal to 100 s.

e. Summary of the source terms for the continuity variables

The source terms for the five continuity variables are as follows.

For water vapor:

$$\frac{dq_v}{dt} = -[\text{PCOND} + \text{PBERG} + \text{PSUB} + \text{PREVP} + \text{PSEVP}]. \quad \text{(A46)}$$

For cloud water:

$$\frac{dq_c}{dt} = \text{PCOND} + \omega\text{PBERG} + \text{PSMLTI} - \text{PRAUT} - \text{PRACW} - \text{PSACW}. \quad \text{(A47)}$$

For rain:

$$\frac{dq_r}{dt} = \text{PREVP} + \text{PRAUT} + \text{PRACW} + \text{PSMLTS}. \quad \text{(A48)}$$

For cloud ice:

$$\frac{dq_i}{dt} = \text{PSUB} + (1 - \omega)\,\text{PBERG} - \text{PSMLTI} - \text{PSAUT} - \text{PSACI}. \quad \text{(A49)}$$

For snow:

$$\frac{dq_s}{dt} = \text{PSEVP} + \text{PSACI} - \text{PSMLTS} + \text{PSACW} + \text{PSAUT}. \quad \text{(A50)}$$

In (A47) and (A49), ω is the weight that partitions the condensed water between cloud water and cloud ice in

the temperature range $T_{00} \leq T < T_0$ (refer to section 2).

Similarly, the source term for T is

$$\frac{dT}{dt} = \frac{L_c}{c_p}(\text{PCOND} + \text{PREVP}) + \frac{L_m}{c_p}(\text{PBERG}) + \frac{L_s}{c_p}(\text{PSUB} + \text{PSEVP}) + \frac{L_f}{c_p}(-\text{PSMLTI} - \text{PSMLTS} + \text{PSACW}), \quad \text{(A51)}$$

where L_m is the modified latent heat of sublimation in the mixed-phase temperature range and is given by

$$L_m = L_c + (1 - \omega) L_f. \quad \text{(A52)}$$

Using (A46) to (A50), it is obvious that under the three-phase processes, total moisture is conserved, or

$$\frac{d}{dt}(q_v + q_c + q_r + q_i + q_s) = 0. \quad \text{(A53)}$$

f. Conservation of the generalized moist static energy

The generalized moist static energy is defined as

$$E = c_pT + gz + L_cq_v - L_f(q_i + q_s), \quad \text{(A54)}$$

where z is the geopotential height. Following Lord (1982), the conservation equation for the generalized moist static energy may be derived as follows. Multiplying (A46) by L_v and (A51) by c_p, and adding them together yields

$$\frac{d}{dt}(c_pT + gz + L_vq_v) = L_f(\text{PSUB} + \text{PSEVP} - \text{PSMLTS} - \text{PSMLTI} + \text{PSACW}) + (L_m - L_v)\,\text{PBERG}, \quad \text{(A55)}$$

using the relation $L_s = L_c + L_f$. Multiplying (A49) and (A50) by L_f and adding them together, we obtain

$$\frac{d}{dt}(L_f(q_i + q_s)) = L_f(\text{PSUB} + \text{PSEVP} - \text{PSMLTS} - \text{PSMLTI} + \text{PSACW}) + L_f(1 - \omega)\,\text{PBERG}. \quad \text{(A56)}$$

Finally, combining (A55) and (A56) leads to an expression of the conservation of the moist static energy under the three-phase processes:

$$\frac{d}{dt}[c_pT + L_cq_v + gz - L_f(q_i + q_s)] = 0. \quad \text{(A57)}$$

Under (A57), it is assumed that there is no variation in moist static energy.

APPENDIX B

List of Symbols

Symbol	Description	Value	Units
A'	Thermodynamic term in PREVP		m s kg^{-1}
A''	Thermodynamic term in PSEVP		m s kg^{-1}
a'	Constant in linear fall speed relation for rain	3×10^3	s^{-1}
a''	Constant in fall speed relation for snow	1.139	m$^{(1-b)}$ s^{-1}
a_0	Coefficient in polynomial fall speed relation for rain	-0.267	m s^{-1}
a_1	Coefficient in polynomial fall speed relation for rain	5.15×10^3	s^{-1}
a_2	Coefficient in polynomial fall speed relation for rain	-1.0225×10^6	m^{-1} s^{-1}
a_3	Coefficient in polynomial fall speed relation for rain	7.55×10^7	m^{-2} s^{-1}
B'	Thermodynamic term in PREVP		m s kg^{-1}
B''	Thermodynamic term in PSEVP		m s kg^{-1}
b	Fall speed exponent for snow	0.11	
C	Capacitance of ice crystal		F
c_p	Specific heat of air at constant pressure	1.005×10^3	J kg^{-1} K^{-1}
D_R	Raindrop diameter		m
D_S	Snowflake diameter		m
E_{RC}	Rain/cloud water collection efficiency	1	
E_{SC}	Snow/cloud water collection efficiency	1	
E_{SI}	Snow/cloud ice collection efficiency	0.1	
e_{sm}	Interpolated saturation vapor pressure		N m^{-2}
e_{si}	Saturation vapor pressure over ice		N m^{-2}
e_{sw}	Saturation vapor pressure over water		N m^{-2}
F	Ventilation factor for rain		

APPENDIX B (*Continued*)

Symbol	Description	Value	Units
F'	Ventilation factor for snow		
FCR	Rate coefficient for collection of cloud water by rain		kg kg^{-1} s^{-1}
FCS	Rate coefficient for collection of cloud water by snow		kg kg^{-1} s^{-1}
FIS	Rate coefficient for collection of cloud ice by snow		kg kg^{-1} s^{-1}
FRV	Rate coefficient for evaporation of rain		kg kg^{-1} s^{-1}
FSV	Rate coefficient for evaporation of snow		kg kg^{-1} s^{-1}
g	gravitational acceleration	9.81	m s^{-2}
K_a	Thermal conductivity of air	2.43×10^{-2}	J m^{-1} s^{-1} K^{-1}
L_c	Latent heat of condensation of water substance	2.5×10^{6}	J kg^{-1}
L_f	Latent heat of fusion of water substance	0.3336×10^{6}	J kg^{-1}
L_s	Latent heat of sublimation of water substance	2.8336×10^{6}	J kg^{-1}
L_m	Modified latent heat of sublimation of water substance in the mixed-phase temperature range		J kg^{-1}
M_w	Molecular weight of water	18.0160	
$M(D_R)$	Mass of raindrop of diameter D_R		kg
$M(D_S)$	Mass of snowflake of diameter D_S		kg
$N_{DR}dD_R$	Number concentration of raindrops with diameters between D_R and $D_R + dD_R$		m^{-3}
$N_{DS}dD_S$	Number concentration of snowflakes with diameters between D_S and $D_S + dD_S$		m^{-3}
N_{0R}	Intercept value in raindrop size distribution	8×10^{6}	m^{-4}
N_{0S}	Intercept value in snowflake size distribution	8×10^{6}	m^{-4}
p_0	Reference pressure level	10^{5}	N m^{-2}
p	Pressure level		N m^{-2}
PBERG	Deposition of water vapor/sublimation of condensate in the mixed phase temperature range.		kg kg^{-1} s^{-1}
PCOND	Condensation of water vapor to cloud water–evaporation of cloud water to water vapor		kg kg^{-1} s^{-1}
PRACW	Collection of cloud water droplets by rain		kg kg^{-1} s^{-1}
PRAUT	Autoconversion of cloud water droplets to rain		kg kg^{-1} s^{-1}
PREVP	Evaporation of rain		kg kg^{-1} s^{-1}
PSACI	Collection of cloud ice crystals by snow		kg kg^{-1} s^{-1}
PSACW	Collection of cloud water droplets by snow		kg kg^{-1} s^{-1}
PSAUT	Autoconversion of cloud ice crystals by snow		kg kg^{-1} s^{-1}
PSEVP	Evaporation of snow		kg kg^{-1} s^{-1}
PSMTLI	Melting of cloud ice to form cloud water		kg kg^{-1} s^{-1}
PSMLTS	Melting of snow to form rain		kg kg^{-1} s^{-1}
PSUB	Deposition of water vapor to cloud ice/sublimation of cloud ice to water vapor		kg kg^{-1} s^{-1}
q_{c0}	Threshold for autoconversion of cloud water to rain	0.25×10^{-3}	kg kg^{-1}
q_c	Mixing ratio of cloud water		kg kg^{-1}
q_{i0}	Threshold for autoconversion of cloud ice to snow	0.01×10^{-3}	kg kg^{-1}
q_i	Mixing ratio of cloud ice		kg kg^{-1}
q_r	Mixing ratio of rain		kg kg^{-1}
q_s	Mixing ratio of snow		kg kg^{-1}
q_{sm}	Interpolated saturation mixing ratio in the mixed-phase temperature range		kg kg^{-1}
q_{si}	Saturation mixing ratio with respect to ice		kg kg^{-1}
q_{sw}	Saturation mixing ratio with respect to water		kg kg^{-1}
q_v	Mixing ratio of water vapor		kg kg^{-1}
R^*	Universal gas constant	8.314×10^{3}	J kmol^{-1} K^{-1}
R_e	Reynolds number		
S_c	Schmidt number	0.6	
S_i	Saturation over ice		

APPENDIX B (*Continued*)

Symbol	Description	Value	Units
S_m	Interpolated saturation in the mixed-phase temperature range		
S_w	Saturation over water		
T_{00}	Lowest threshold temperature for supercooled cloud water to form	253.16	K
T_0	Threshold temperature for melting of cloud ice and snow	273.16	K
T	Temperature		K
t	Time		s
$\bar{V}$	Mass-weighted fall speed of precipitation		$m\ s^{-1}$
V_R	Mass-weighted fall speed for rain		$m\ s^{-1}$
$V_R(D_R)$	Fall speed of raindrop of diameter D_R		$m\ s^{-1}$
V_S	Mass-weighted fall speed for snow		$m\ s^{-1}$
$V_S(D_S)$	Fall speed of snowflake of diameter D_S		$m\ s^{-1}$
α	Rate coefficient for autoconversion of cloud water	0.01	s^{-1}
β	Rate coefficient for autoconversion of cloud ice	0.001 at T_0	s^{-1}
χ	Diffusivity of water vapor in air	2.26×10^{-5}	$m^2\ s^{-1}$
Γ	Gamma function		
ϵ_0	Permittivity of free space	8.854×10^{-12}	$C^2\ N^{-1}\ m^{-2}$
λ_R	Slope of rain size distribution		m^{-1}
λ_S	Slope of snow size distribution		m^{-1}
μ	Dynamic viscosity of air	1.718×10^{-5}	$kg\ m^{-1}\ s^{-1}$
π		3.1416	
π^*	Pressure scale		
ρ	Density of air		$kg\ m^{-3}$
ρ_L	Density of water	10^3	$kg\ m^{-3}$
ρ_S	Density of snow	10^2	$kg\ m^{-3}$
τ_i	Relaxation time for condensation–evaporation	100	s
τ_m	Relaxation time for deposition–sublimation in the mixed-phase temperature range	100	s
τ_w	Relaxation time for deposition–sublimation	100	s
ω	Weight for interpolation of the saturation vapor pressure in the mixed phase temperature range		

REFERENCES

Arakawa, A., 1975: Modelling clouds and cloud processes for use in climate models. GARP Publication Series No. 16, ICSU/WMO, 183–197.

——, and W. H. Schubert, 1974: The interactions of a cumulus cloud ensemble with the large-scale environment. Part I: *J. Atmos. Sci.*, **31,** 674–701.

Bauer, P., and P. Schluessel, 1993: Rainfall, total water, ice water, and water vapor over sea from polarized microwave simulations and Special Sensor Microwave/Imager data. *J. Geophys. Res.*, **98,** 20 737–20 759.

Beard, K. V., and H. R. Pruppacher, 1971: A wind tunnel investigation of the rate of evaporation of small water droplets falling at terminal velocity in air. *J. Atmos. Sci.*, **28,** 1455–1464.

Bergeron, T., 1935: On the physics of clouds and precipitation. *Proc. Fifth Assembly UGGI,* Lisbon, 2.

Betts, A. K., and Harshvardhan, 1987: Thermodynamic constraint on the cloud liquid water feedback in climate models. *J. Geophys. Res.*, **92,** 8483–8485.

Bougeault, P., 1981: Modelling the trade-wind cumulus boundary layer. Part I: Testing the ensemble cloud relations against numerical data. *J. Atmos. Sci.*, **38,** 2414–2428.

——, 1985: A single parameterization of the large-scale effects of deep cumulus convection. *Mon. Wea. Rev.*, **113,** 2108–2221.

Byers, H. R., 1965: *Elements of Cloud Physics.* University of Chicago Press, 191 pp.

Charlock, T. P., 1982: Cloud optical feedback and climate stability in a radiative–convective model. *Tellus,* **34,** 245–254.

——, K. M. Cattany-Carnes, and F. Rose, 1988: Fluctuation statistics of outgoing longwave radiation in a general circulation model and in satellite data. *Mon. Wea. Rev.*, **116,** 1540–1554.

Coiffier, J., Y. Ernie, J. F. Geleyn, J. Clochard, J. Hoffman, and F. Dupont, 1987: The operational hemispheric model at the French Meteorological Service. *J. Meteor. Soc. Japan,* Spec. NWP Symp. Vol., 337–345.

Cotton, W. R., M. A. Stephens, T. Nehrkorn, and G. J. Tripoli, 1982: The Colorado State University three-dimensional cloud/mesoscale model—1982. Part II: An ice phase parameterization. *J. Rech. Atmos.*, **16,** 295–320.

Del Genio, A. D., and M.-S. Yao, 1988: Sensitivity of a global climate model to the specification of convective updraft and downdraft mass fluxes. *J. Atmos. Sci.*, **45,** 2641–2668.

——, and ——, 1990: Predicting cloud water variations in the GISS GCM. Preprints, *Conf. on Cloud Physics,* San Francisco, CA, Amer. Meteor. Soc., 497–504.

Ebert, E. E., and J. A. Curry, 1992: A parameterization of ice cloud optical properties for climate models. *J. Geophys. Res.*, **97,** 3831–3836.

Feigelson, E. M., 1978: Preliminary radiation model of a cloudy atmosphere. Part I: Structure of clouds and solar radiation. *Contrib. Atmos. Phys.*, **51,** 203–229.

Flatau, P. J., G. J. Tripoli, J. Verlinde, and W. R. Cotton, 1989: The CSU-RAMS cloud microphysics module. General theory and documentation. Atmos. Sci. Paper 451, Dept. Atmos. Sci., Colorado State University, Fort Collins, Colorado, 88 pp.

Foote, G. B., and P. S. Du Toit, 1969: Terminal velocity of raindrops aloft. *J. Appl. Meteor.*, **8,** 249–253.

Fowler, L. D., and D. A. Randall, 1994: A global radiative convective feedback. *Geophys. Res. Lett.*, **21,** 2035–2038.

——, and ——, 1996: Liquid and ice cloud microphysics in the CSU general circulation model. Part II: Impact on cloudiness, the earth's radiation budget, and the general circulation of the atmosphere. *J. Climate,* **9,** 530–560.

Ghan, S. J., and R. C. Easter, 1992: Computationally efficient approximations to stratiform cloud microphysics parameterization. *Mon. Wea. Rev.*, **120,** 1572–1582.

——, C. C. Chuang, and J. E. Penner, 1993: A parameterization of cloud droplet nucleation. Part I: Single aerosol type. *Atmos. Res.*, **30,** 198–221.

——, ——, R. C. Easter, and J. E. Penner, 1995: A parameterization of cloud droplet nucleation. Part II: Multiple aerosol types. *Atmos. Res.*, **36,** 39–54.

Greenwald, T. J., G. L. Stephens, T. H. Vonder Haar, and D. L. Jackson, 1993: A physical retrieval of cloud liquid water over the global oceans using Special Sensor Microwave/Imager (SSM/I) observations. *J. Geophys. Res.*, **98,** 18 471–18 448.

Gunn, K. L. S., and G. D. Kinzer, 1949: The terminal velocity of fall for water droplets in stagnant air. *J. Meteor.*, **6,** 243–251.

——, and J. S. Marshall, 1958: The distribution with size of aggregate snow flakes. *J. Meteor.*, **15,** 452–461.

Hansen, J., G. Russel, D. Rind, P. Stone, A. Lacis, S. Lebedeff, R. Ruedy, and L. Travis, 1983: Efficient three-dimensional global models for climate studies: Models I and II. *Mon. Wea. Rev.*, **111,** 609–662.

Harshvardhan, and D. A. Randall, 1985: Comments on "The parameterization of radiation for numerical weather prediction." *Mon. Wea. Rev.*, **113,** 1832–1833.

——, ——, T. G. Corsetti, and D. A. Dazlich, 1989: Earth radiation budget and cloudiness simulations with a general circulation model. *J. Atmos. Sci.*, **46,** 1922–1942.

Heise, E., 1984: Experiments with the Sasamori- and the ECWMF cloud cover and liquid water content parameterization. *Proc. of Workshop on Cloud Cover Parameterization in Numerical Models,* Reading, U.K., ECWMF, 109–131.

Heymsfield, A. J., and L. J. Donner, 1990: A scheme for parameterizing ice-cloud water content in general circulation models. *J. Atmos. Sci.*, **47,** 1865–1877.

Holloway, J. L., Jr., and S. Manabe, 1971: Simulation of climate by a global general circulation model. *Mon. Wea. Rev.*, **99,** 335–370.

Houze, R. A., P. V. Hobbs, P. H. Herzegh, and D. B. Parsons, 1979: Size distributions of precipitation particles in frontal clouds. *J. Atmos. Sci.*, **36,** 156–162.

Hu, Y. X., and K. Stamnes, 1993: An accurate parameterization of the radiative properties of water cloud suitable for use in climate models. *J. Climate,* **6,** 728–742.

Kessler, E., III, 1969: On the distribution and continuity of water substance in atmospheric circulations. *Meteor. Monogr.,* No. 32, Amer. Meteor. Soc., 84 pp.

Kuo, H. L., 1965: On the formation and intensification of tropical cyclones through latent release by cumulus convection. *J. Atmos. Sci.*, **22,** 40–63.

Laval, K., H. Le Treut, and R. Sadourny, 1981: Effect of cumulus parameterization on the dynamics of a general circulation model. *Geophys. Astrophys. Fluid Dyn.*, **17,** 113–127.

Legates, D. R., and C. J. Willmott, 1990: Mean seasonal and spatial variability in gauge-corrected global precipitation. *Int. J. Climatol.*, **10,** 111–127.

Le Treut, H., and Z.-X. Li, 1988: Using Meteosat data to validate a prognostic cloud generation scheme. *Atmos. Res.*, **21,** 273–292.

Lin, B., and W. B. Rossow, 1994: Observations of cloud liquid water path over oceans: Optical and microwave remote sensing methods. *J. Geophys. Res.*, **99,** 20 907–20 928.

Lin, Y.-L., R. D. Farley, and H. D. Orville, 1983: Bulk parameterization of the snow field in a cloud model. *J. Climate Appl. Meteor.*, **22,** 1065–1092.

Liou, K.-N., and G. D. Wittman, 1979: Parameterization of the radiative properties of clouds. *J. Atmos. Sci.*, **36,** 1261–1273.

Locatelli, J. D., and P. V. Hobbs, 1974: Fallspeeds and masses of solid precipitation particles. *J. Geophys. Res.*, **79,** 2185–2197.

Lord, S. J., 1982: Interaction of a cumulus cloud ensemble with the large-scale environment. Part III: Semi-prognostic test of the Arakawa–Schubert cumulus parameterization. *J. Atmos. Sci.*, **39,** 88–103.

——, W. C. Chao, and A. Arakawa, 1982: Interaction of a cumulus ensemble model with the large-scale environment. Part IV: The discrete model. *J. Atmos. Sci.*, **39,** 104–113.

Manabe, S., J. Smagorinsky, and R. F. Strickler, 1965: Simulated climatology of a general circulation model with a hydrological cycle. *Mon. Wea. Rev.*, **93,** 769–798.

Marshall, J. S., and W. McK. Palmer, 1948: The distribution of raindrop with size. *J. Meteor.*, **5,** 165–166.

McAvaney, B. J., W. Bourke, and K. Puri, 1978: A global spectral model for simulation of the general circulation. *J. Atmos. Sci.*, **35,** 1557–1583.

McFarlane, N. A., G. J. Boer, J. P. Blanchet, and M. Lazare, 1992: The Canadian Climate Centre second-generation general circulation model and its equilibrium climate. *J. Climate,* **5,** 1013–1044.

Mellor, G. L., 1977: The Gaussian cloud model relation. *J. Atmos. Sci.*, **34,** 356–358.

Morcrette, J.-J., 1991: Radiation and cloud radiative properties in the European Centre for Medium-Range Weather Forecasting system. *J. Geophys. Res.*, **96,** 9121–9132.

Njoku, E. G., and L. Swanson, 1983: Global measurements of sea surface temperature, wind speed, and atmospheric water content from satellite microwave radiometry. *Mon. Wea. Rev.*, **111,** 1977–1987.

Ose, T., 1993: An examination of the effects of explicit cloud water in the UCLA GCM. *J. Meteor. Soc. Japan,* **71,** 93–109.

Paltridge, G. W., 1980: Cloud–radiation feedback to climate. *Quart. J. Roy. Meteor. Soc.*, **106,** 895–899.

Platt, C. M. R., and Harshvardhan, 1988: The temperature dependence of cirrus extinction: Implications for climate feedbacks. *J. Geophys. Res.*, **93,** 11 051–11 058.

Prabhakara, C., I. Wang, A. T. C. Chang, and P. Gloersen, 1983: A statistical examination of *Nimbus-7* SMMR data and remote sensing of sea surface temperature, liquid water content in the atmosphere, and surface wind speed. *J. Climate Appl. Meteor.*, **22,** 2023–2037.

Pruppacher, H. R., and J. D. Klett, 1978: *Microphysics of Clouds and Precipitation.* D. Reidel, 714 pp.

Randall, D. A., 1987: Turbulent fluxes of liquid water and buoyancy in partly cloudy layers. *J. Atmos. Sci.*, **44,** 850–858.

——, 1989: Cloud parameterization for climate modeling: Status and prospects. *Atmos. Res.*, **23,** 341–361.

——, and D. A. Dazlich, 1991: Diurnal variability of the hydrologic cycle in a general circulation model. *J. Atmos. Sci.*, **48,** 40–62.

——, and D.-M. Pan, 1993: Implementation of the Arakawa–Schubert cumulus parameterization with a prognostic closure. *The Representative of Cumulus Convection in Numerical Models, Meteor. Monogr.,* No. 46 Amer. Meteor. Soc., 137–144.

——, Harshvardhan, D. A. Dazlich, and T. G. Corsetti, 1989: Interactions among radiation, convection, and large-scale dynamics in a general circulation model. *J. Atmos. Sci.*, **46,** 1943–1970.

——, Q. Shao, and C.-H. Moeng, 1992: A second-order boundary-layer model. *J. Atmos. Sci.*, **49,** 1903–1923.

Raschke, E., J. Schmetz, J. Heintzenberg, R. Kandel, and R. W. Saunders, 1990: The International Cirrus Experiment (ICE). A joint european effort. *Eur. Space Agency,* **14,** 193–199.

Ricard, J. L., and J. F. Royer, 1993: A statistical cloud scheme for use in a AGCM. *Ann. Geophys.*, **11,** 1095–1115.

Roeckner, E., M. Rieland, and E. Keup, 1990: Modelling of clouds and radiation in the ECHAM model. *Proc. of ECMWF/WCRP Workshop on Clouds, Radiation, and the Hydrologic Cycle,* ECMWF, Reading, UK, 199–222.

Rutledge, S. A., and P. V. Hobbs, 1983: The mesoscale and microscale structure and organization of clouds and precipitation in midlatitude cyclones. VIII: A model for the "seeder–feeder" process in warm-frontal rainbands. *J. Atmos. Sci.,* **40,** 1185–1206.

——, and ——, 1984: The mesoscale and microscale structure and organization of clouds and precipitation in midlatitude cyclones. XII: A diagnostic modeling study of precipitation development in narrow cold-frontal rainbands. *J. Atmos. Sci.,* **41,** 2949–2972.

Sasamori, T., 1975: A statistical model for stationary atmospheric cloudiness, liquid water content, and rate of precipitation. *Mon. Wea. Rev.,* **103,** 1037–1049.

Sellers, P. J., Y. Mintz, Y. C. Sub, and A. Dalcher, 1986: A simple biosphere model (SiB) for use within general circulation models. *J. Atmos. Sci.,* **43,** 505–531.

——, J. A. Berry, G. J. Collatz, C. B. Field, D. A. Randall, C. J. Tucker, C. O. Justice, and O. S. Los, 1993: Modeling land surface atmosphere fluxes of energy, moisture and carbon on global scales. *Proc., Conf. on Hydroclimatology,* Anaheim, CA., Amer. Meteor. Soc., 41–42.

Senior, C. A., and J. F. B. Mitchell, 1993: Carbon dioxide and climate: The impact of cloud parameterization. *J. Climate,* **6,** 393–418.

Slingo, A., Ed., 1985: Handbook of the Meteorological Office 11-layer atmospheric general circulation model., Rep. DCTN, 29, Meterol. Off., Bracknell, U.K..

——, 1989: A GCM parameterization for the shortwave radiative properties of water clouds. *J. Atmos. Sci.,* **46,** 1419–1427.

Smagorinsky, J., 1960: On the dynamical prediction of large-scale condensation by numerical methods. *Physics of Precipitation, Geophys. Monogr.,* Amer. Geophys. Union, **5,** 727–768.

——, S. Manabe, and J. L. Holloway Jr., 1965: Numerical results of a nine-level general circulation model. *Mon. Wea. Rev.,* **93,** 727–768.

Smith, R. N. B., 1990: A scheme for predicting layer clouds and their water content in a general circulation model. *Quart. J. Meteor. Soc.,* **116,** 435–460.

Smith, L. D., and T. H. Vonder Haar, 1991: Clouds–radiation interactions in a general circulation model: Impact upon the planetary radiation balance. *J. Geophys. Res.,* **96,** 893–914.

——, and D. A. Randall, 1992: Parameterization of cloud microphysical processes in the CSU General Circulation Model. Atmos. Sci. Paper 491, Dept. Atmos. Sci., Colorado State University, Fort Collins, CO, 58 pp.

Somerville, R. C. J., and L. A. Remer, 1984: Cloud optical thickness feedbacks in the CO_2 climate problem. *J. Geophys. Res.,* **89,** 9668–9672.

Sommeria, G., and J. W. Deardorff, 1977: Sub-grid scale condensation in models of nonprecipitating clouds. *J. Atmos. Sci.,* **34,** 344–355.

Stephens, G. L., 1978: Radiation profiles in extended water clouds. Part II: Parameterization schemes. *J. Atmos. Sci.,* **35,** 2123–2132.

Suarez, M. J., A. Arakawa, and D. A. Randall, 1983: Parameterization of the planetary boundary layer in the UCLA general circulation model: Formulation and results. *Mon. Wea. Rev.,* **111,** 2224–2243.

Sundqvist, H., 1978: A parameterization scheme for non-convective parameterization including prediction of cloud water content. *Quart. J. Roy. Meteor. Soc.,* **104,** 677–690.

——, 1993: Inclusion of ice phase of hydrometeors in cloud parameterization for mesoscale and largescale models. *Contrib. Atmos. Phys.,* **66,** 137–147.

——, E. Berge, and J. E. Kristjansson, 1989: Condensation and cloud parameterization studies with a mesoscale numerical weather prediction model. *Mon. Wea. Rev.,* **117,** 1641–1657.

Tiedtke, M., 1989: A comprehensive mass flux scheme for cumulus parameterization in large-scale models. *Mon. Wea. Rev.,* **117,** 1779–1800.

——, 1993: Representation of clouds in large-scale models. *Mon. Wea. Rev.,* **121,** 3040–3061.

Washington, W. M., and A. Kasahara, 1970: A January simulation experiment with the two-layer version of the NCAR global circulation model. *Mon. Wea. Rev.,* **98,** 559–580.

Wetherald, R. T., and S. Manabe, 1988: Cloud feedback processes in a general circulation model. *J. Atmos. Sci.,* **45,** 1397–1415.

Weinstein, A. I., 1970: A numerical model of cumulus dynamics and microphysics. *J. Atmos. Sci.,* **27,** 246–255.

Williamson, D. L., J. T. Kiehl, V. Ramanathan, R. E. Dickinson, and J. J. Hack, 1987: Description of the NCAR Community Climate Model (CCM1). Tech. Note NCAR/TN-285+STR, Natl. Center for Atmos. Res., Boulder, CO, 112 pp.

Xu, K.-M., and D. A. Randall, 1994: Further development of a cloud parameterization for use in climate models with ARM data. *Fifth Symp. on Global Change Studies.* Nashville, TN, Amer. Meteor. Soc., 6–10.